American Mineralogist, Volume 108, pages 70–86, 2023

Fe^{3+}/Fe^{T} ratios of amphiboles determined by high spatial resolution single-crystal synchrotron Mössbauer spectroscopy

Barbara C. Ratschbacher[1,2,*], Jennifer M. Jackson[1], Thomas S. Toellner[3], Claire E. Bucholz[1], Wolfgang Sturhahn[1], and Natalia V. Solomatova[4]

[1]Division of Earth and Planetary Sciences, California Institute of Technology, 1200 E. California Boulevard, Pasadena, California 91125, U.S.A
[2]Department of Earth and Planetary Sciences, University of California, Davis, One Shields Avenue, Davis, California 95616, U.S.A
[3]Argonne National Laboratory, 9700 South Cass Avenue, Argonne, Illinois 60439, U.S.A.
[4]Laboratoire de Géologie de Lyon, École Normale Supérieure de Lyon, CNRS UMR 5276, 46 Allée d'Italie, Lyon 69364, France

Abstract

The Fe^{3+}/Fe^{T} ratios ($Fe^{3+}/[Fe^{2+}+Fe^{3+}]$) in minerals can be used to understand their crystallization and post-crystallization conditions. However, as natural minerals are often zoned and contain inclusions, bulk techniques, e.g., wet chemistry, may not provide accurate Fe^{3+}/Fe^{T} values for a single phase of interest. We determined Fe^{3+}/Fe^{T} ratios of amphiboles in different crystallographic orientations by single-crystal synchrotron Mössbauer spectroscopy (SMS) in energy and time domain modes from four volcanic localities (Long Valley Caldera, Mount St. Helens, Lassen Volcanic Center, U.S.A., and Mt. Pinatubo, Philippines). The high spatial resolution (as low as 12 × 12 μm spot size) and standard-free nature of SMS allow the detection of intra-grain compositional heterogeneities in Fe^{3+}/Fe^{T} with relatively low uncertainties.

We combine SMS with major element compositions, water contents, and hydrogen isotope compositions to document the Fe^{3+}/Fe^{T} ratios as a function of mineral composition and post-crystallization dehydrogenation. Spectra were fitted with up to five distinct sites: ferrous iron on M(1), M(2), M(3), and ferric iron on M(2) and M(3), consistent with X-ray diffraction studies on single crystals of amphibole. The Fe^{3+}/Fe^{T} ratios range from 0.14 ± 0.03 (Long Valley Caldera), 0.51 to 0.63 ± 0.02 (representing intra-grain heterogeneities, Mount St. Helens) to 0.86 ± 0.03 (Lassen Volcanic Center). The latter grain experienced post-crystallization dehydrogenation, shown by its low water content (0.6 ± 0.05 wt%) and its elevated hydrogen isotope composition (δD = +25 ± 3‰ relative to SMOW). The Fe^{3+}/Fe^{T} ratios of 0.62 ± 0.01 and 0.20 ± 0.01 of two Mt. Pinatubo grains correlate with high-Al_2O_3 cores and low-Al_2O_3 rims and smaller phenocrysts in the sample, respectively. This study shows that SMS is capable of distinguishing two different domains with dissimilar Fe^{3+}/Fe^{T} values formed under different crystallization conditions, demonstrating that SMS in combination with major element, water, and hydrogen isotope compositions allows the interpretation of amphibole Fe^{3+}/Fe^{T} ratios in the context of crystallization and post-crystallization processes.

Keywords: Amphibole, Mössbauer spectroscopy, Fe^{3+}/Fe^{T} ratios, dehydrogenation

Introduction

Amphiboles are common minerals in hydrous mafic to felsic arc magmas (e.g., Hawthorne and Oberti 2007; Krawczynski et al. 2012). Due to their common occurrence and stability over wide pressure, temperature, and compositional ranges, the chemistry of amphiboles has been used to infer processes such as magma mixing and recharge (e.g., Kiss et al. 2014; Barnes et al. 2016; Zou and Ma 2020) and to reconstruct the pressure and temperature histories of volcanic and plutonic rocks (e.g., Humphreys et al. 2019; Peters et al. 2017; Mutch et al. 2016; Johnson and Rutherford 1989).

Amphiboles incorporate both ferrous (Fe^{2+}) and ferric iron (Fe^{3+}) into their crystal structure. Thus, the Fe^{3+}/Fe^{T} ratio has the potential to record the oxygen fugacity of the melt from which they crystallized (e.g., King et al. 2000). However, the use of Fe^{3+}/Fe^{T} ratios in natural amphiboles as potential indicators of magma chemistry requires their accurate determination. Bulk techniques such as wet chemistry and conventional Mössbauer spectroscopy suffer from potentially averaging intra-grain compositional variability and inclusions occurring in natural amphiboles, thus posing a challenge to accurately reflect the conditions during amphibole crystallization. A high spatial resolution technique with low uncertainties is required to understand amphibole Fe^{3+}/Fe^{T} ratios in the context of their magmatic history.

We characterize volcanic amphiboles by single-crystal, synchrotron Mössbauer spectroscopy, an analytical technique that provides the spatial resolution to avoid averaging heterogeneous grains and to detect intra-grain Fe^{3+}/Fe^{T} ratio variations. Furthermore, it uses the physics of nuclear forward scattering on single crystals (e.g., Sturhahn and Gerdau 1994; Sturhahn 2000, 2004), and therefore it does not require reference spectra for data interpretation as required for other techniques determining Fe^{3+}/Fe^{T} ratios (e.g., X-ray absorption near edge structure spectroscopy; Dyar et al. 2016). Moreover, synchrotron-based Mössbauer spectroscopy is time-efficient compared to conventional Mössbauer spectroscopy. Herein, we investigate calcic

* E-mail: barbara.ratschbacher@gmail.com. Orcid 0000-0002-2112-7225

0003-004X/23/0001–070$05.00/DOI: https://doi.org/10.2138/am-2022-8115

amphiboles from four volcanic localities. We determine their major and minor element composition (electron microprobe), water content and hydrogen isotope composition (secondary-ion mass spectrometry), unit-cell parameters (X-ray diffraction), and Fe^{3+}/Fe^{T} ratios, using time- and energy-domain synchrotron-based Mössbauer spectroscopy at the Advanced Photon Source at Argonne National Laboratory, U.S.A. We discuss our results in the context of amphibole mineral chemistry as well as crystallization and post-crystallization processes.

Samples

Four volcanic samples were selected for this study. Sample MC18-2 is from a lava flow sampled at the West Moat coulee (age 161 ± 2 ka; Hildreth 2004) in the Long Valley Caldera (California, U.S.A.) and thus part of the post-caldera rhyolitic flows following the Bishop tuff eruption (~760 ka), which created the Long Valley Caldera (e.g., Hildreth and Mahood 1986; Crowley et al. 2007). Sample LF02-042 is from a lava flow from the Kings Creek sequence (Underwood et al. 2012) of the Lassen Volcanic Center (LVC) in northern California. The LVC marks the southernmost part of the Cascades arc; the Lassen Domefield represents the final stage of the LVC and contains ~35 ka biotite- and hornblende-bearing rhyodacites located in the Kings Creek and Hat Creek areas east of Lassen Peak (e.g., Turrin et al. 1998; Clynne and Muffler 2010). Sample SH315-4 was collected from a dacite lava spine ejected during the 2004 to 2006 crystal-rich and gas-poor eruption at Mount St. Helens (U.S.A.) (e.g., Pallister et al. 2008; Thornber et al. 2008). Sample PH13A (two grains analyzed from this sample) is a phenocryst-poor dacite pumice, which erupted as part of the cataclysmic eruption in June 1991 at Mt. Pinatubo, a prominent stratovolcano in the Bataan segment of the Taiwan-Luzon arc in the Philippines (e.g., Pallister et al. 1996).

Methodology

Sample preparation

Amphiboles were separated using a jaw crusher and a Frantz Isodynamic Magnetic Separator. Individual grains were crushed to <700 µm, handpicked under a binocular microscope, mounted in epoxy, and polished for analysis by electron microprobe (EMPA) and secondary-ion mass spectrometry (SIMS). Most grains are fragments of whole grains to maximize the total integrated intensities while avoiding thickness effects. Analyses of thinner grains are possible but require longer data collection times, especially if samples are not enriched in ^{57}Fe. Based on backscatter electron images and chemical compositions, we selected grains with the fewest inclusions and alteration and/or decomposition features. One grain was selected from each sample, except for sample PH13A, from which we selected two grains (PH13A A1 and PH13A A2). After EMPA and SIMS analysis, we removed the grains from the epoxy and glued them on a micromesh for single-crystal X-ray diffraction (XRD) analysis. Finally, the grains were glued with a known orientation on a Plexiglas slide for SMS analyses. After SMS analyses, grain PH13A A1 was removed from the Plexiglas slide and pressed in indium for the second set of water analyses by SIMS. Grain PH13A A2 is the only grain that was analyzed by SIMS only after SMS analyses. The details of each of these steps are described below.

Electron microprobe analysis

Major and minor elements in amphibole were determined using a JEOL JXA-8200 electron microprobe at the California Institute of Technology after each grain was imaged in electron backscatter mode. Multiple points (transects through entire grains) were analyzed on each individual grain to map intra-grain compositional variations. We used an acceleration voltage of 15 kV, a beam current of 25 nA, and a defocused beam of 10 µm diameter, analyzing Si, Al, Mg, Ca, Na, K, Fe, Mn, Ti, F, and Cl with counting times set to 20 s for each element and 10 s for the background. The following standards were used to calibrate the elemental peaks prior to analyzing the unknowns: forsterite, Shankland P-658 (Mg), fayalite RDS P-1086 (Fe), Mn olivine RDS P-1087 (Mn), synthetic anorthite (Si, Al, Ca), Amelia albite (Na), asbestos microcline (K), synthetic TiO_2 (Ti), synthetic Cr_2O_3 (Cr), synthetic F-phlogopite (F), and synthetic sodalite (Cl). Data reduction was performed by a modified ZAF procedure (CITZAF; Armstrong 1995). The detection limits were ≤0.01 wt% for SiO_2, Al_2O_3, MgO, TiO_2, CaO, K_2O, and Cl; ≤0.02 wt% for FeO, Na_2O, Cr_2O_3, MnO, and F. The EMPA analysis results and their 1σ uncertainties (percent of absolute values) calculated from counting statistics are listed in Online Materials[1] Table OM1.

Secondary-ion mass spectrometry

Water concentrations and D/H ratios were obtained on a Cameca 7f-GEO SIMS at the California Institute of Technology where such analysis of H_2O and D/H ratios are routinely performed on nominally anhydrous minerals (olivine, pyroxene, plagioclase; Mosenfelder et al. 2011; Chin et al. 2016), apatite (e.g., Boyce et al. 2010; Treiman et al. 2016), melt inclusions (Taylor et al. 2016; Ni et al. 2017) with well-established analytical protocols. We developed a new but similar protocol for our amphiboles. Two natural amphiboles (magnesio-hastingsite from Kipawa, Canada; H_2O: 1.45 ± 0.19 wt%; δD: –88 ± 10‰ (relative to SMOW), and a magnesio-arfvedsonite from Ilimaussaq, Greenland: H_2O: 1.45 ± 0.12 wt%; δD: –142 ± 10‰), previously characterized for their water contents and D/H ratios by Deloule et al. (1991), were used as reference materials. Anhydrous olivine from the Springwater meteorite served to determine background H_2O. The latter can reach ≤1 ppm for epoxy-free sample mounts, ~10 ppm for polished thin sections, and tens to hundreds of parts per million for epoxy mounts. Although we mounted our amphiboles in epoxy, the high H_2O concentrations in our amphiboles made the background corrections insignificant. In addition, the sample mounts were kept for >48 h at 10^{-9} torr in the sample chamber prior to analysis to reduce the background signal. For the H_2O analysis, a focused, 10 keV Cs^+ primary beam of 4–5 nA (~15 µm in diameter) was used to pre-sputter the sample in rastering (10 × 10 µm) mode for 120 s. The raster size was reduced to 5 × 5 µm during sample data acquisition. ^{12}C, $^{17}O/^{1}H$, and $^{18}O/^{1}H$ were sequentially measured on an electron multiplier in the peak-jumping mode for 20 cycles, with 1 s counting times for each mass. We used a mass resolving power (MRP) of 5500 to remove the ^{17}O interference from $^{18}O/^{1}H$. The hydrogen isotope analyses were performed after the H_2O analyses in the same area of the sample, with similar beam conditions. Because of the low-$^{2}H^-$ counting rate, a large field aperture (300 µm) was used. Secondary ions ($^{1}H^-$, $^{2}H^-$) were collected using a MRP of 500 for 20 cycles on the samples and 40 cycles on the reference materials. In each cycle, the counting times were 1 s for $^{1}H^-$ and 8 s for $^{2}H^-$. Typical σ_{mean} uncertainties (percent of absolute values) were at ~8% for water concentrations and included the counting statistical error of each point and the propagated error from the calibration line determined from the standards. For hydrogen isotopic measurements, the errors of the δD values include the counting statistical error of each individual measurement and the standard deviation of repeated analysis of the standards. The measurements (including counts, uncorrected, and corrected data) are listed in Online Materials[1] Table OM1.

Single-crystal X-ray diffraction

We conducted single-crystal X-ray diffraction experiments at the X-ray Crystallography Facility in the Beckman Institute at the California Institute of Technology, using either a Bruker AXS D8 VENTURE four-circle diffractometer with molybdenum or copper *K*α radiation from a IμS micro source or a Bruker AXS KAPPA APEXII four-circle diffractometer using Mo*K*α radiation from a sealed-tube X-ray generator. The XRD data sets represent coverage of reciprocal space in between that needed for a typical orientation matrix and a full crystal structure refinement. The latter is required to solve for atomic positions and exclude the presence of micro-twinning but requires a sample at most 100 µm in size to minimize the amount of crystal in the beam. This is much smaller than the several hundred micrometer-sized grains selected for our study. A large grain size was preferred to analyze potential Fe^{3+} heterogeneity within single amphibole grains using SMS. Therefore, we cannot rule out the presence of micro-twinning in some of our grains.

APEX3 software (Bruker 2012a) was used for fitting diffraction peaks and refining lattice parameters. In addition, we used the CELL_NOW program (Bruker 2012b) to index the unit cell. In situ video collection was used to identify crystal faces for each grain. All experiments were conducted at room temperature.

The collection of XRD data had three goals: (1) to determine the unit-cell parameters and correlate them with Fe^{3+}/Fe^{T} ratios; (2) to exclude crystals that reveal large-domain twinning and/or contain inclusions; and (3) to index crystal faces to

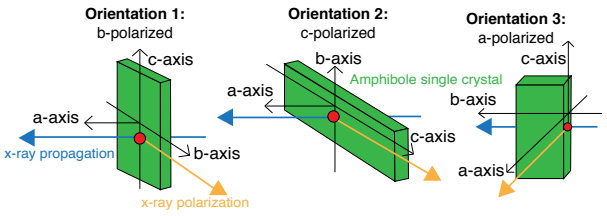

Figure 1. Schematic illustration of the single-crystal orientations relative to the X-ray propagation and polarization directions. Note these are transmission measurements. The canting angle describes the orientation of the crystal axes with respect to the X-ray propagation direction and is 0° in orientation 1 and 3 and 90° in orientation 2 (see text for explanation and fit of canting angle). These directions are not always along principal crystallographic directions. The exact propagation direction is given in Online Materials[1] Table OM1 for each grain. (Color online.)

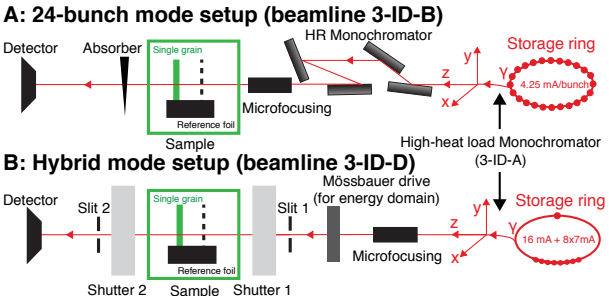

Figure 2. Schematic illustration of the nuclear forward scattering setups at sector 3, Advanced Photon Source, Argonne National Laboratory. The sample is rotated along its crystallographic axes to collect time-domain synchrotron-Mössbauer spectra along different orientations (Fig. 1). In setup B, a Mössbauer drive can be inserted before slit 1 to allow for data collection in the energy domain. Setup B allows to collect a longer delay-time spectra compared to setup A and with a higher incident beam power density (A: 1.7×10^7 photon/s/μm² vs. B: 1.0×10^{10} ph/s/μm²). Both setups use a high-heat load monochromator in station 3ID-A as indicated in the schematic. (Color online.)

control the orientation of the X-ray propagation and polarization directions relative to the crystallographic axes of the single crystal during SMS measurements. Each grain was glued onto a Plexiglas slide in a known orientation for SMS analyses. The Plexiglas could then be rotated relative to the X-ray propagation and polarization directions to analyze different orientations (Fig. 1).

Single-crystal synchrotron Mössbauer spectroscopy

Mössbauer spectroscopy (MS) yields information on the valence state, local bonding, and magnetism of ^{57}Fe in a solid through hyperfine interactions of the Fe nucleus with its environment and their influence on the absorption and re-emission of γ rays (e.g., Margulies and Ehrman 1961; Sturhahn and Gerdau 1994; Fultz 2002; Sturhahn 2004, 2005; Dyar et al. 2006; Sturhahn and Jackson 2007; Vandenberghe and De Grave 2013). It is worth noting the advantages of time-resolved synchrotron Mössbauer spectroscopy. For example, the brightness of the source for SMS is very high (~10^{23} photons/s/eV/sr), compared with radioactive sources used for conventional Mössbauer spectroscopy (100 mCi ^{57}Co source: ~10^{13} photons/s/eV/sr). The signal-to-noise ratio (S/N, or quality) of SMS spectra is also very high. The SMS measurements of the amphibole samples reported here produce very high signal-to-noise ratio spectra (~10^3:1, for amphiboles with counting rates ~20 to 30 Hz and a detector background level measured at ~0.02 Hz) compared with radioactive sources used for conventional Mössbauer spectroscopy (~10^{-2}:1 for 100 mCi ^{57}Co source) (e.g., Sturhahn 2004). The quality of the spectra can be understood based on the information contained in a given spectrum. The very low-S/N value for conventional Mössbauer spectroscopy can be understood based upon determining the total area of the absorption peaks (resonant signal originating from the sample) and comparing it with the total area of the spectrum. Note that wider velocity-ranges lead to lower S/N. That is, a significant fraction of the data acquired in such a measurement is non-resonant, i.e., background. In an SMS measurement, every photon detected is a signal. The S/N for SMS is high not because the counting rates are so high but because the background is extremely low.

For single crystals, the collection of synchrotron Mössbauer time spectra along distinct crystallographic orientations (Fig. 1) yields additional constraints due to the linear polarized nature of synchrotron radiation and the inherent polarization dependence of the hyperfine interactions. This sample-orientation dependence in single-crystal time spectra helps to disentangle and identify contributions from numerous crystallographically distinct ferric and ferrous ^{57}Fe sites in amphiboles. More discussion on the comparison between time- and energy-domain Mössbauer spectroscopy can be found in Sturhahn (2004) and references therein.

SMS measurements were performed at beamline 3ID of the Advanced Photon Source at Argonne National Laboratory. Three different measurement setups were used to collect SMS spectra of amphibole single crystals. These setups uniquely allow us to arrive at the best possible model of hyperfine parameters for these amphibole grains by collecting spectra: (1) in the time and energy domain using the linear polarized nature and very high brightness of a synchrotron radiation source and (2) in the time-domain with delay times up to ~450 ns, and (3) with an efficient use of beamtime. These setups operate with different filling patterns in the storage ring (24-bunch mode and hybrid mode) and different X-ray optics to provide a stable beam of 14.4 keV photons. Time calibration was performed for each set of measurements. The setups are described here.

(1) 24-bunch mode setup. These measurements were performed at station B at beamline 3ID using a setup similar to previous studies (e.g., Solomatova et al. 2019; Fig. 2a). Synchrotron radiation from the beamline's undulator has its band width reduced to 2eV (full-width at half maximum, FWHM) centered at 14.413 keV using a LN2-cooled silicon double-crystal monochromator. A secondary, high-resolution monochromator reduces the bandwidth further to 1 meV (FWHM) (Toellner 2000). X-rays were then focused on the sample to a spot size of 20 × 20 μm². An optical microscope allowed the positioning of the X-ray beam on approximately the same spot used for the EMPA and SIMS measurements. An avalanche photodiode detector and conventional time-filtering electronics were used to collect time spectra in the forward direction between delay times of around 22 to 120 ns, dependent on storage ring filling quality. The incident beam power density (flux density) on the sample was 1.7×10^7 ph/s/μm². The collection time for one orientation varied between 1 to 3 h, dependent on the grain thickness, the Fe content, and the hyperfine fields.

(2) Hybrid mode setup using high-speed shutters: Time-domain. These measurements were performed at station D at beamline 3ID using a new spectrometer (Toellner et al. 2011) that implements a pair of high-speed shutters to extract the SMS signal using the single bunch of the hybrid mode as the excitation pulse (Fig. 2b). It operates without a high-resolution monochromator. The beam was focused on the sample with a spot size of 12 × 12 μm with a flux density of 1.0×10^{10} ph/s/μm². The spectra measured in this mode have an accessible time window that is significantly longer compared to the 24-bunch mode but begins at delay times of >60 ns. Despite the capability of measuring long delay times, our samples typically produced little signal beyond approximately 210–450 ns. In addition, this dual-shutter setup achieves higher counting rates than during the 24-bunch mode, which significantly reduces measurement time and is an advantage for samples with low amounts of ^{57}Fe.

(3) Hybrid mode setup using high-speed shutters: Energy-domain. The setup is similar to the hybrid mode time-domain setup described above but includes a Mössbauer drive (with a single-line resonant material) inserted between the microfocusing optics and shutter 1 (Fig. 2b). A 10 μm thick 304-grade stainless steel foil (natural abundance of ^{57}Fe) was used as the single-line emitter. An absorption spectrum of the sample convolved with that of the single-line emitter was measured by collecting the radiation transmitted through the sample as a function of the velocity, or Doppler shift, of the Mössbauer drive. The velocity calibration of the drive was performed using the known spectrum of an α-Fe foil. The scan range of the two collected energy-domain spectra varied between +4 to –4 mm/s and +6 to –6 mm/s. Spectra were collected for 12 h each with a spot size of 12 × 12 μm.

Data collection procedures

For each amphibole grain, we collected time spectra with and without a well-characterized stainless steel (SS) reference foil (natural isotopic distribution of ^{57}Fe; thickness of 5 or 10 μm). Collection times are a function of Fe content and sample thickness; for grain-only, they are between ~1 to 3 h and ~1 h for the grain with

the SS reference foil. The foil was secured and placed in the upstream direction as a reference absorber to determine the isomer shift, which is strongly sensitive to the oxidation state of iron. A time spectrum of a grain was always followed by a spectrum of the grain with SS foil. In the 24-bunch mode setup, we collected up to three sets of spectra with delay time windows of about 22 to 120 ns for different crystallographic orientations (Fig. 1). We specify crystal orientations in terms of (1) the lattice planes (*hkl*) that were oriented perpendicular to the incident X-ray beam during the SMS measurements and therefore perpendicular to the X-ray propagation vector, and (2) the direction of polarization. For grains MC18-2, SH315-4, and PH13A-A2, we placed an aperture on the grain to ensure fiducial placement of the X-rays. The aperture is a Cu strip with a ~100 μm diameter opening drilled into it using an electric discharge machine, which facilitates locating the center of the aperture by scanning across its width, guaranteeing that exactly the same spot was analyzed for the first and second orientations. For grains LF02-042 and PH13A A1, no aperture was used, but data were also collected in a third crystallographic orientation (Fig. 1). Online Materials[1] File OM1 lists the number of spectra and collection time for each sample for different orientations and with different modes. On grain SH315-4, data from two additional areas were collected to evaluate intra-grain compositional heterogeneity.

In hybrid mode, time spectra with delay times ranging from 60 to 350 ns (1 h collection time) and 100 to 500 ns (overnight collection time) were measured for at least one crystallographic orientation. For grains MC18-2 and SH315-4, energy domain spectra were also collected.

Crystal chemistry of iron in amphiboles

The amphibole formula can be written as $AB_2C_5T_8O_{22}W_2$ (Hawthorne and Oberti 2007), with A, B, C, and T referring to groups of cations occupying specific sites in the structure. There are three distinct octahedrally coordinated M sites that are occupied by C cations, M(1), M(2), and M(3), and one site, M(4), that is occupied by B cations. Amphiboles incorporate Fe^{2+} and Fe^{3+} only in octahedral coordination (B and C cations). Iron in tetrahedral coordination (T cations) has not been documented (Hawthorne and Oberti 2007). Few studies performed conventional MB spectroscopy and a complete structural refinement from single-crystal XRD data on amphiboles (e.g., Redhammer and Roth 2002; Driscall et al. 2005; Abdu and Hawthorne 2009; Uvarova et al. 2007; Oberti et al. 2018). These studies provide information about site preferences of Fe^{2+} and Fe^{3+}: Fe^{3+} strongly prefers the M(2) site, whereas Fe^{2+} dominates the M(1) and M(3) sites but can also occur on the M(4) site. The preference for Fe^{2+} is M(1)>M(3)>>M(2), although Oberti et al. (2007) documented a random distribution between the M(1) and M(3) sites for amphiboles crystallized at high temperatures. In calcic amphiboles, Fe^{2+} may occupy the M(4) site (e.g., Goldman and Rossman 1977), but as discussed below, a Fe^{2+} M(4) site is not necessary to achieve a good fit for the SMS spectra in this study. Ferric iron only occurs on the M(2) site in amphiboles with a fully occupied W = $(F,Cl,OH)_2$ site but can occur at M(1), M(2), and M(3) in amphiboles with an oxo-component (O at the W-site in addition to F, Cl, and OH; Oberti et al. 2007). The oxidation of Fe^{2+} to Fe^{3+} on the M(1) and M(3) sites is the major mechanism for achieving local bond-valence satisfaction during the loss of hydrogen from the structure and the formation of the oxo-component (dehydrogenation; e.g., Oberti et al. 2007; Della Ventura et al. 2018).

Defining the Mössbauer sites and spectral fitting

Computing the Euler angles. We define six distinct Mössbauer sites (MB sites) corresponding to the M(1), M(2), M(3) sites, which can be each occupied by Fe^{3+} and/or Fe^{2+}. These are as follows: Fe^{2+} on M(1); Fe^{2+} on M(2); Fe^{2+} on M(3); Fe^{3+} on M(1); Fe^{3+} on M(2); Fe^{3+} on M(3). We note that introducing a Fe^{2+} M(4) site in our model does not improve the fitting of our spectra (see Results section).

For each of the M(1), M(2), and M(3) sites, which can be occupied by Fe^{2+} and/or Fe^{3+}, unique Euler angles can be calculated that describe the orientation of the electric field gradient at the ^{57}Fe nucleus with respect to the orientation of the single crystal. By calculating Euler angles for each MB site (see below), we clearly define and relate each MB site to a crystallographic site via atomic parameters. Thus, each site's contribution to the overall spectrum is distinguishable. We used published atomic parameters of each site (MB and non-MB sites; Online Materials[1] Table OM2) of a magnesio-hornblende amphibole with a similar major element composition as our amphiboles (Makino and Tomita 1989). We combined these parameters with unit-cell base vectors and angles from the XRD analyses and the EMPA data, from which we can allocate cations and anions to crystallographic sites to define each site and its cation and or anion occupation. The "kvzz" executable in the CONUSS (COherent NUclear resonant Scattering by Single crystals) software package (Sturhahn 2000; http://www.nrixs.com) allows calculating the main axes of the electric field gradient from the local symmetry around the iron nucleus and thus the calculation of the Euler angles. The "kvzz" executable requires defining each MB and non-MB site not only by the atomic parameters but also by its occupation and site weight. For example: there are five C cations in the amphibole structure: Ti, Al, Mn, Fe, Mg; grain SH315-4 has 2.03 apfu Fe on the C sites and shares these with 0.09 apfu Ti, 0.41 apfu Al, and 2.47 apfu Mg (adding up to 5 apfu); thus, the total Fe-site weight is 0.40. There are six distinct MB sites, three Fe^{2+} and three Fe^{3+} sites corresponding to M(1), M(2), and M(3), thus each MB site has a site weight of 0.07. Amphibole grains vary in major element composition, which influences site weights, average bond lengths, and unit-cell parameters, and, therefore the Euler angles. However, these variations have a minimal effect on the calculated angles; for example, variations of 0.5 apfu Fe on the C sites and a ≤0.1 Å difference between unit-cell base vectors only change the Euler angles by <0.132°. The Euler angles are listed in Online Materials[1] Table OM3.

Establishing a starting model for spectral fitting. Conventional MB studies also provide information about the range of hyperfine parameters of Fe^{2+} and Fe^{3+}. We compiled hyperfine parameters from conventional MB studies on amphiboles and use these as a guide to constrain our fitting models (see Online Materials[1] File OM4 for data and references). In general, Fe^{3+} shows quadrupole splitting (QS) between 0.25 to 1.70 mm/s compared to 1.19 to 2.93 mm/s for Fe^{2+} (Online Materials[1] Table OM4). The isomer shift (IS; with respect to α-Fe) for Fe^{3+} is close to 0.4 mm/s (Online Materials[1] Table OM4). The IS for Fe^{2+} is between 0.97 to 1.28 mm/s (Online Materials[1] Table OM4). All studies report that the Fe^{3+} M(3) site has a higher QS than the other Fe^{3+} sites. Similarly, the Fe^{2+} M(1) site has a higher QS than the other Fe^{2+} sites. However, conventional MB spectroscopy proves challenging to ascribe Fe^{3+} and Fe^{2+} to specific crystallographic sites. Therefore, we do not let our models be constrained by these values; instead we use these ranges as guidelines for a starting model to fit our data.

Fitting the data. We fitted our SMS spectra using version

2.2.1 of the CONUSS software package (Sturhahn 2021). All fitted spectra incorporate the transmission integral (Margulies and Ehrman 1961; Sturhahn and Gerdau 1994). We used the dual fit module, which allows simultaneous fittings of data with and without the reference SS foil. We aimed to develop a single-crystal chemical model in CONUSS that best fits all individual spectra of each grain.

The recoil-free fraction, also known as the Lamb-Mössbauer factor f_{LM}, is used to fit the data in the CONUSS software package. We used an estimated but reasonable value of the Lamb-Mössbauer factor of 0.75 to fit our amphibole data. Highly accurate values of the average f_{LM} can be obtained, for example, by conducting nuclear resonant inelastic X-ray scattering measurements (NRIXS) on the phase of interest (e.g., Murphy et al. 2013; Morrison et al. 2019; Ohira et al. 2021) or on materials that have similar valence and coordination environments and are at similar *P-T* conditions. High statistical quality NRIXS measurements on unenriched samples like the amphiboles studied here require several days (to a week or more), as we would need to isolate the much smaller zone-free region of the grains. Our estimated value of 0.75 is reasonable considering values determined for minerals containing octahedrally coordinated ferrous (enstatite: 0.709 ± 0.003 for En_{80} to 0.723 ± 0.003 for En_{93}, Jackson et al. 2009) and octahedrally coordinated ferric iron in hydrous minerals (goethite: 0.77, Dauphas et al. 2012; uncertainties were not provided). If one assumes these cited end-member values given here, the resulting effect on the Fe^{3+}/Fe^{T} ratio is within the cited uncertainties.

CONUSS was also used to pre-determine the optimal grain thickness before multiple-scattering effects dominate the measured spectrum. This guided our selection of suitable grains for SMS analysis. The "kfor" executable computes the local effective thickness and Online Materials[1] Table OM3 lists the local effective thicknesses for the various data sets. Except for the third orientation of grains LF02-042 and PH13A A1, all values are <1, thus, thickness effects are not expected.

For data fitting, we use the "kmco" executable in CONUSS, which entails a Monte Carlo sampling approach to explore the parameter space. This has been done within the starting model parameter range (see section above) as well as outside these ranges to explore whether better fits can be achieved. Refinements of fits have been carried out using the "kctl" executable in CONUSS.

Imperfect alignment of the grain's principle crystallographic axes with the X-ray propagation direction as a result of minimal tilting of the grain during mounting on the plexiglass slide causes a deviation in the canting angle from 0° in orientations 1 and 3 and 90° in orientation 2 (Fig. 1). Fitting of the canting angle resulted in a maximum deviation of 23° from the expected values and can be explained by this misalignment.

The presence of fractures and/or strain in our crystals, potentially acquired during eruption, as well as twinning, have an impact on the texture coefficient. A texture coefficient of 100% is expected for perfect single crystals, indicating no randomly orientated hyperfine fields. The presence of micro-twinning, impossible to detect from the limited "orientation matrix" XRD data we collected, can account for a texture coefficient below 100%. Thus, in a final step of fitting, we varied the texture coefficient, which led to improved consistency of fits for the different orientations. Different texture coefficients would be expected for different orientations (24-bunch mode data; Fig. 1) as the orientation of the micro-twin(s) with respect to the larger grain is difficult to constrain. Imperfect alignment of the grain (discussed above) can also partly explain a texture coefficient below 100%.

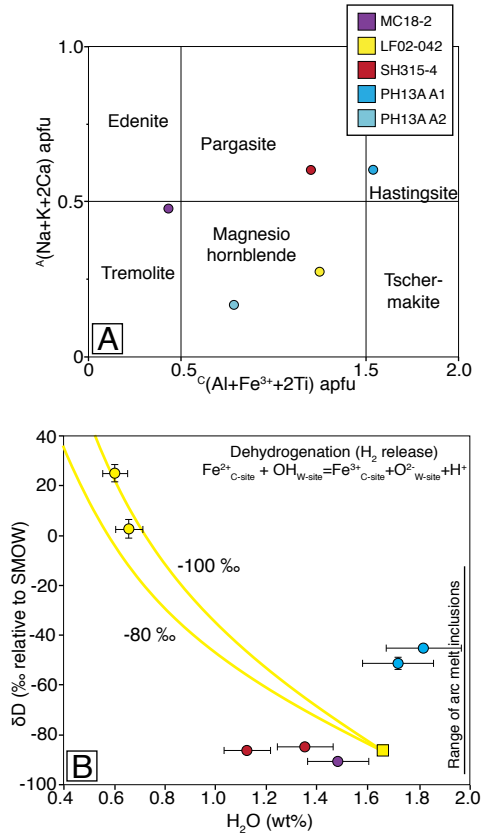

Figure 3. (**a**) Nomenclature of amphiboles following Hawthorne et al. (2012). Ferric iron content determined by synchrotron Mössbauer spectroscopy; (**b**) water content (wt%) and δD (in ‰ relative to SMOW) of amphiboles determined by secondary-ion mass spectrometry. The yellow lines show a Rayleigh fractionation model indicating the trend caused by H_2 release (dehydrogenation) in amphiboles (fractionations of –100‰ and –80‰). The starting composition of the model (yellow square) has 1.65 wt% H_2O and a δD composition of –86 ‰. The range of arc melt inclusions is from Shaw et al. (2008) and Walowski et al. (2015). See text for details. Errors are smaller than the symbol size if not shown. (Color online.)

Results

Amphibole major element compositions, water content, and δD

Amphibole colors observed in thin section range from green-brown to yellow-red. A red color in volcanic amphiboles was attributed to post-crystallization iron oxidation during eruption and cooling via H_2 loss [i.e., dehydrogenation; e.g., Dyar et al. (1993); Miyagi et al. (1998)]. LF02-042 shows a red color, whereas grains MC18-2, SH315-4, PH13A A1, and PH13A A2

have no reddish color (Online Materials[1] Fig. OM1 shows thin section images of each sample).

The amphiboles examined here are calcic amphiboles [nomenclature after Hawthorne et al. (2012) shown in Fig. 3a]. Grain MC18-2 contains inclusions of feldspar, magnetite, and apatite (Fig. 4a); LF02-042 and PH13A A2 have no inclusions at the surface (Figs. 4b and 4e); SH315-4 has magnetite inclusions and is discolored along fractures and around inclusions (Fig. 4c); PH13A A1 includes magnetite at its edges (Fig. 4d).

FeO contents in amphiboles are ~20 wt% (MC18-2), ~18 wt% (SH315-4), ~13 wt% (PH13A A2), and ~12 wt% (LF02-042; Fig. 4). Grain PH13A A1 shows intra-grain compositional variability: Al_2O_3 decreases from 12 wt% in the interior (brighter area in the BSE image) to 7–8 wt% in the rim (darker area; Fig. 4d). CaO also decreases from the core (12 wt%) to rim (8–9 wt%). FeO decreases from 13 wt% at spot 1 to 10 wt% at spot 12 (Fig. 4d). The intra-grain variability in the other grains is minor and is <1 wt% for each oxide (Fig. 4). Grain PH13A A2 shows brighter and darker areas in the BSE image but lacks changes in major element compositions (Fig. 4e). The water contents are 1.82 ± 0.15 to 1.72 ± 0.14 wt% (PH13A A1), 1.51 ± 0.12 to 1.55 ± 0.13 wt% (PH13A A2; determined after SMS data collection), 1.47 ± 0.12 (MC18-2), 1.35 ± 0.1 to 1.12 ± 0.09 (SH315-4), and 0.65–0.60 ± 0.5 (LF02-042; Figs. 3 and 4). After SMS analysis, grain PH13A A1 was removed from the Plexiglas slide and fixed in indium for a second water-content analysis. The water contents in the area of the previous SIMS and the SMS analyses are 1.72 ± 0.12 to 1.91 ± 0.13 wt%, similar to the values measured before SMS analyses. The hydrogen isotope composition of grain MC18-2 is δD = –91 ± 1‰ (Fig. 4a). LF02-042 shows heavier values in the center (δD = +25 ± 3‰) than at the edge (δD = +2.7 ± 4‰; Fig. 4b). SH315-4 shows similar values in two areas: –84 ± 1‰ and –86 ± 2‰ (Fig. 4c). PH13A A1 has a slightly lighter composition in its center (δD = –51 ± 2‰) than its edge (δD = –45 ± 2‰; Fig. 4d).

Single-crystal X-ray diffraction

Unit-cell dimensions of our amphiboles match the range reported for calcic amphiboles (space group *C*2/*m*; Hawthorne and Oberti 2007; Online Materials[1] Table OM1). Cell volumes range from 899 (SH315-4), 907 (PH13A A2), 906 (LF02-042), 911 (PH13A A1), to 915 Å^3 (MC18-2) . Beta angles vary from 104.7° (PH13A A2), 104.8° (MC18-2) to 105.0° (LF02-042), 105.1° (PH13A A1), and 105.5° (SH325-4).

Single-crystal synchrotron Mössbauer spectroscopy

We attempted to fit all spectra for each grain, i.e., those collected in different orientations and during different data collection setups, with a similar model. Spectra were fitted first with a texture coefficient of 100%, i.e., with no randomly orientated hyperfine fields, appropriate for single crystals. In a final step, the texture coefficient was fitted. This yielded improved fits for some spectra. Online Materials[1] Table OM1 lists the best-fit hyperfine parameters, thickness, and canting angles. Online Materials[1] Figure OM2 shows best-fit results of dual fits with data and reference foil. Uncertainties for the weight fractions of the Fe^{2+} and Fe^{3+} sites of each fit reflect correlations between sites and are given in Online Materials[1] Table OM1. The average Fe^{3+}/Fe^{T} ratio for each grain is calculated from

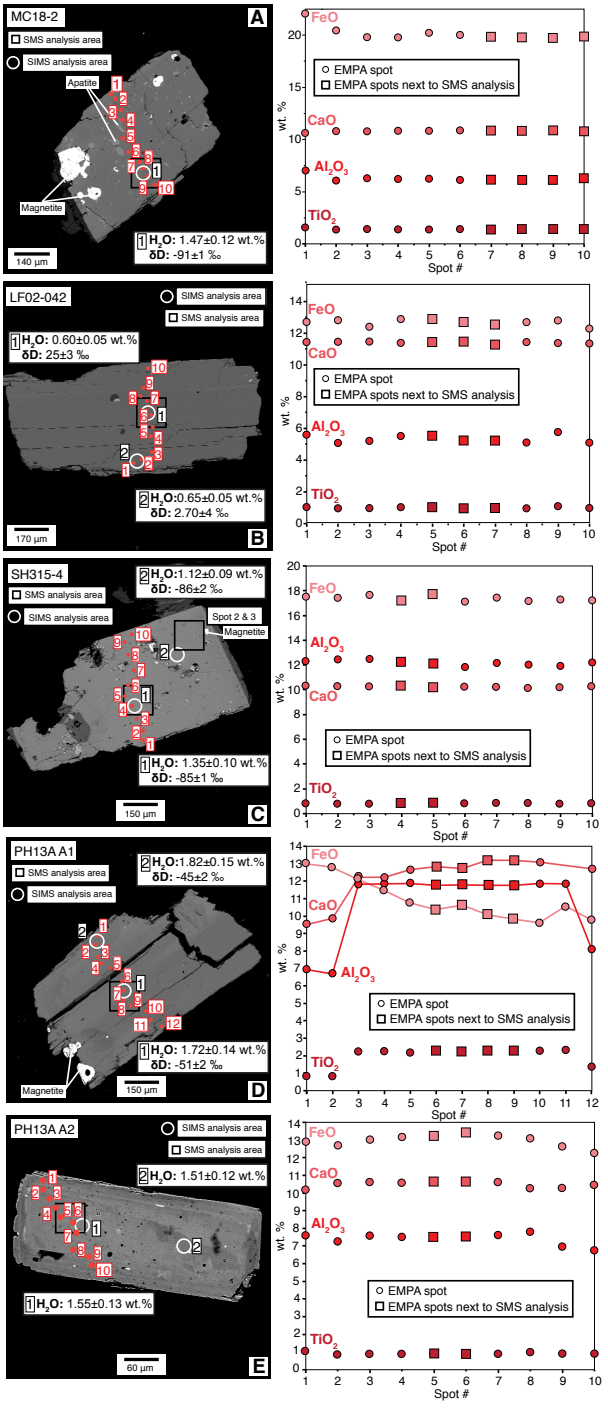

► **Figure 4.** Left side: Backscatter electron images of grains showing electron microprobe and secondary-ion mass spectrometry analysis spots and the areas where SMS spectra were collected. Right side: Variation in major element oxides determined by EMPA along transects through the grains. For uncertainties of EMPA analysis see text. (**a**) MC18-2; (**b**) LF02-042; (**c**) SH315-4; (**d**) PH13A A1; analyzed points are connected by lines for clarity; (**e**) PH13A A2. (Color online.)

spectra collected in the same area and takes into account error propagation. Online Materials[1] Table OM5 shows correlation matrices for grains LF02-042 and MC18-2 as an example of a ferric- and ferrous-rich grain.

Spectra of grain MC18-2 were fitted with five sites; these are (site and site weight): Fe^{2+} M(1) with 10–17%, Fe^{2+} M(2) with 45–55%, Fe^{2+} M(3) with 16–30%, Fe^{3+} M(2) with 2–5%, and Fe^{3+} M(3) with 9–13% (Fig. 5). This combination of sites yielded the lowest χ^2 for both the 24-bunch and hybrid mode spectra. Calculated Fe^{3+}/Fe^{T} ratios are 0.13 ± 0.02 to 0.14 ± 0.02.

Spectra of grain LF02-042 were fitted with four sites: Fe^{2+} M(1) with 8–9%, Fe^{2+} M(3) with 5%, Fe^{3+} M(2) with 46–55%, and Fe^{3+} M(3) with 32–40%. This combination of sites yielded the lowest χ^2 for both the 24-bunch and hybrid mode spectra (Fig. 6) and Fe^{3+}/Fe^{T} ratios of 0.86 ± 0.09 to 0.87 ± 0.12.

Spectra of grain SH315-4 were fitted with five sites: Fe^{2+} M(1) with 12–18%, Fe^{2+} M(2) with 6–7%, Fe^{2+} M(3) with 14–20%, Fe^{3+} M(2) with 25–40%, and Fe^{3+} M(3) with 23–36%. The hybrid time domain spectrum of SH315-4 was fitted with three additional sites: a polycrystalline Fe^{2+} site accounting for twinning at M(2) and M(3), and two sites accounting for disordered magnetic oxides of low weight 1–13%, which occur as inclusions, and observed in the hybrid energy domain spectrum; the Fe^{3+}/Fe^{T} ratios are 0.58 ± 0.02 to 0.63 ± 0.03 (Fig. 7). Spots 2 and 3, analyzed in different areas (Fig. 4c), yielded Fe^{3+}/Fe^{T} ratios of 0.51 ± 0.02 to 0.59 ± 0.02, respectively.

Spectra of grain PH13AA2 were fitted with five sites: Fe^{2+} M(1) with 7–9%, Fe^{2+} M(2) with 52–56%, Fe^{2+} M(3) with 16–19%, Fe^{3+} M(2) with 13–14%, and Fe^{3+} M(3) with 7%. Orientations 1 and 2 analyzed during hybrid mode yielded similar fits (Fig. 8). The Fe^{3+}/Fe^{T} ratios are 0.20 ± 0.03 to 0.21 ± 0.01.

Spectra of grain PH13AA1 were fitted with four sites: Fe^{2+} M(1) with 3–14%, Fe^{2+} M(3) with 22–34%, Fe^{3+} M(2) with 58–61%, and Fe^{3+} M(3) with 1–11%. The Fe^{3+}/Fe^{T} ratios range from 0.61 ± 0.01 to 0.64 ± 0.03 (Fig. 9).

Online Materials[1] Figure OM3 shows additional fitted spectra not displayed in Figures 5 to 9. Additionally, we also calculated energy domain spectra from measured energy domain spectra of MC18-2 and SH315-4 (Figs. 5 and 9) and time domain spectra of PH13AA1 (Fig. 9) using the CONUSS software.

The IS and QS ranges are in general agreement with those determined by conventional Mössbauer spectroscopy (Fig. 10). IS are larger for Fe^{2+} (~0.9–1.2 mm/s; Figs. 10a–10c) than for Fe^{3+} (~0.25–0.45 mm/s; Figs. 10d and 10e). QS of the Fe^{2+} sites of grains SH315-4, MC18-2, PH13AA1, and PH13AA2 increase in the following order: M(1) > M(3) > M(2) in accordance with literature data (Figs. 10a–10c; Online Materials[1] Table OM4). Grain LF02-042 shows a QS at the M(3) site that is larger compared to M(1). QS of the Fe^{3+} M(3) site in this grain is larger compared to the M(2) site in agreement with literature data. The difference in QS between M(3) and M(2) is minimal for grain SH315-4 (Figs. 10d and 10e).

The EMPA, SIMS, and SMS data collected in similar areas on each grain (~50–100 μm²; Fig. 4) allow the correlation of major element composition, Fe^{3+}/Fe^{T} ratio, and water content (oxo-component). An increase in the site weight of Fe^{2+} at M(2) (~0.05 to 0.55 apfu) accompanies an increase of the QS of Fe^{2+} at M(1) and M(3) from ~2.5 to 2.8 mm/s and 2.1 to 2.4 mm/s, respectively (Figs. 11a and 11b). The QS of Fe^{3+} at M(2) decreases from ~0.95 to 0.7 mm/s with increasing magnesium content (Fig. 11c). An increase of the

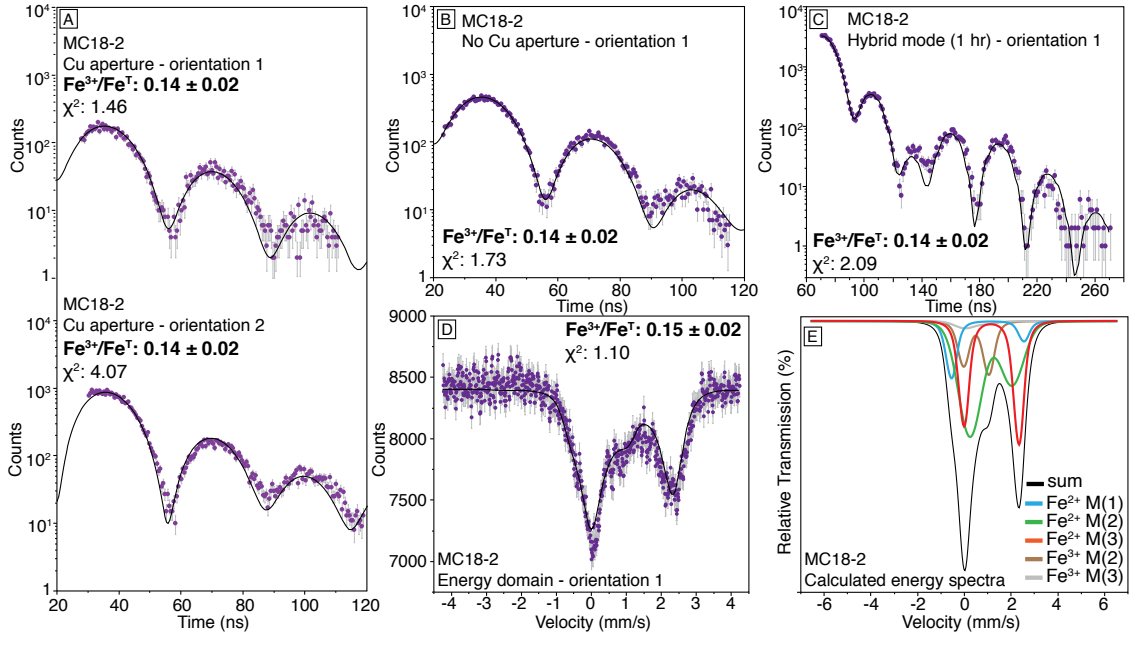

Figure 5. Synchrotron Mössbauer spectra of grain MC18-2: (**a**) 24-bunch mode spectra of orientation 1 and 2 collected with a Cu aperture; (**b**) 24-bunch mode spectra of orientation 1 collected without a Cu aperture; (**c**) hybrid mode time domain spectrum collected for 1 h for orientation 1; (**d**) hybrid mode energy domain spectrum collected for 12 h for orientation 1; (**e**) calculated energy domain data using the best-fit values from **d**. Corresponding best fits are shown with χ^2 for each fit and resulting Fe^{3+}/Fe^{T} ratios. The calculated breakdown of the site doublets and their sum for the energy spectrum uses the best-fit hyperfine parameters, transmission integral, and a linear polarized X-ray source. (Color online.)

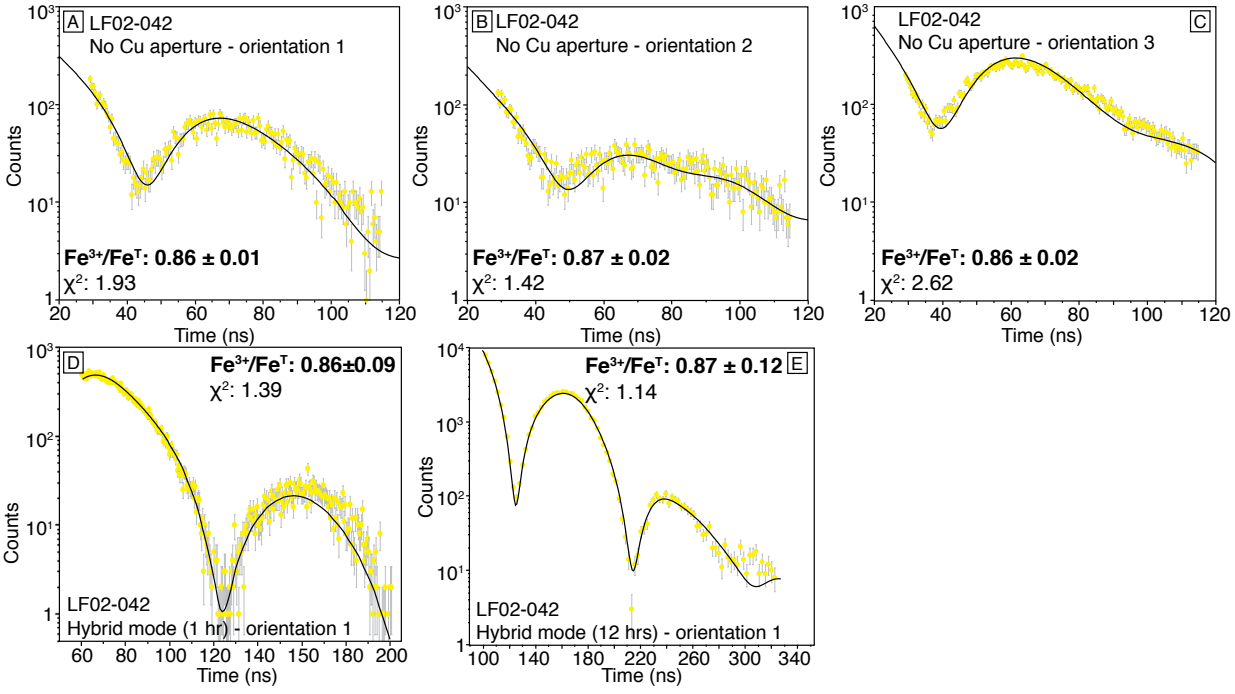

Figure 6. Synchrotron Mössbauer spectra of grain LF02-042: (**a**, **b**, and **c**) 24-bunch mode spectra of orientation 1, 2, and 3; (**d**) hybrid mode time domain spectrum collected for 1 h for orientation 1; (**e**) hybrid mode time domain spectrum collected for 12 h for orientation 1. Corresponding best fits are shown with χ^2 for each fit and resulting Fe^{3+}/Fe^{T} ratios. (Color online.)

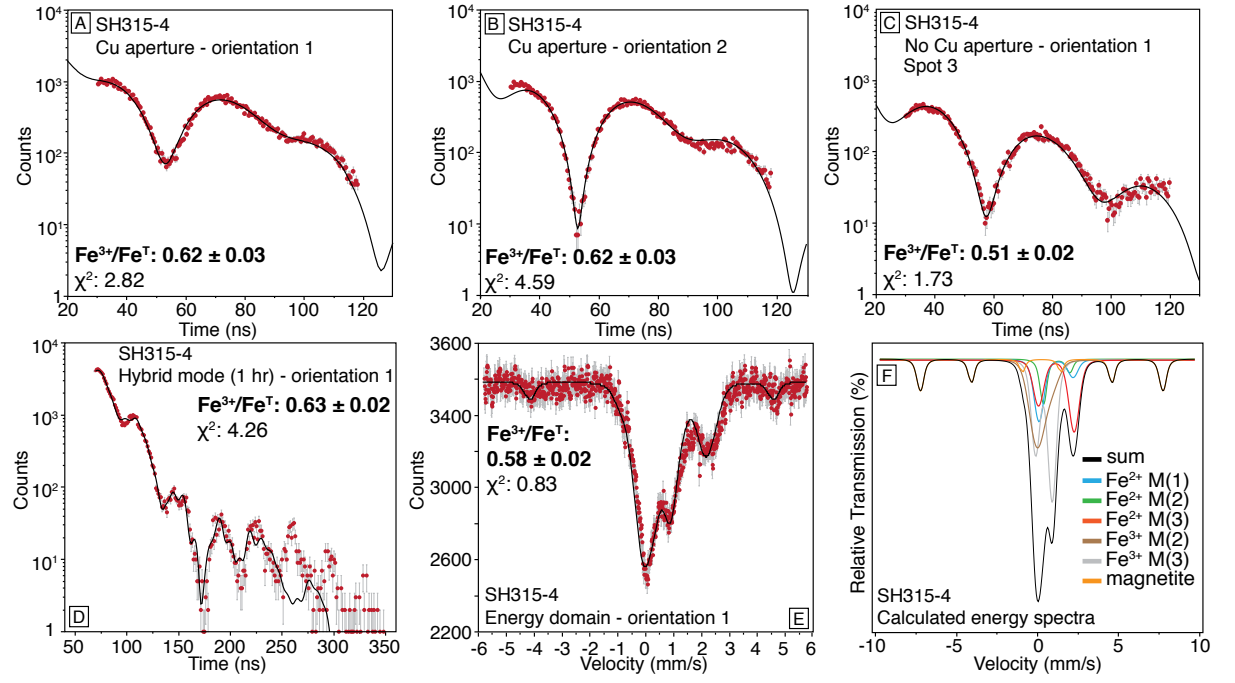

Figure 7. Synchrotron Mössbauer spectra of grain SH315-4: (**a** and **b**) 24-bunch mode spectra of orientation 1 and 2 collected with a Cu aperture; (**c**) 24-bunch mode spectra of spot 3 for orientation 1 (see Fig. 4c for location on the grain); (**d**) hybrid mode time domain spectrum collected for 1 h for orientation 1; (**e**) hybrid mode energy domain spectrum collected for 12 h for orientation 1; (**f**) calculated energy domain data using the best-fit values from **e**. Corresponding best fits are shown with χ^2 for each fit and resulting Fe^{3+}/Fe^{T} ratios. The calculated breakdown of the site doublets and their sum for the energy spectrum uses the best-fit hyperfine parameters, transmission integral, and a linear polarized X-ray source. (Color online.)

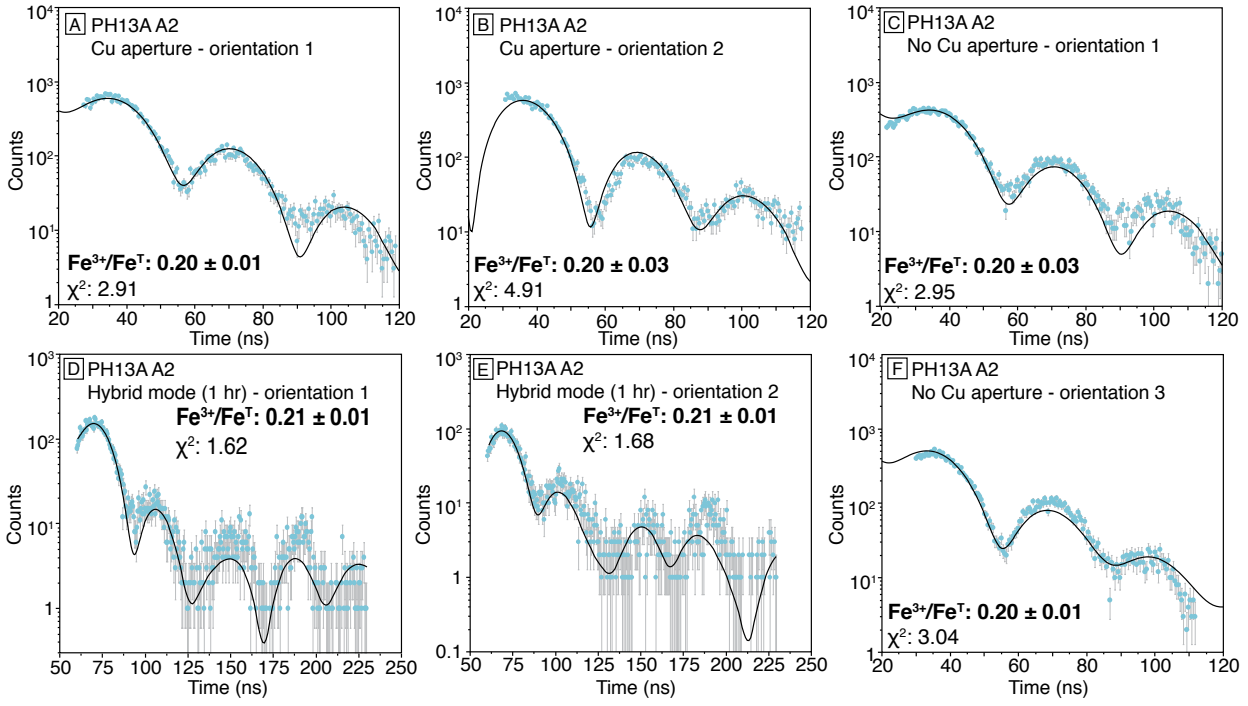

Figure 8. Synchrotron Mössbauer spectra of grain PH13A A2: (**a** and **b**) 24-bunch mode spectra of orientation 1 and 2 collected with a Cu aperture; (**c**) 24-bunch mode spectra of orientation 1; (**d** and **e**) hybrid mode time domain spectrum collected for 1 h for orientation 1 and 2; (**f**) 24-bunch mode spectra of orientation 3. Corresponding best fits are shown with χ^2 for each fit and resulting Fe^{3+}/Fe^{T} ratios. (Color online.)

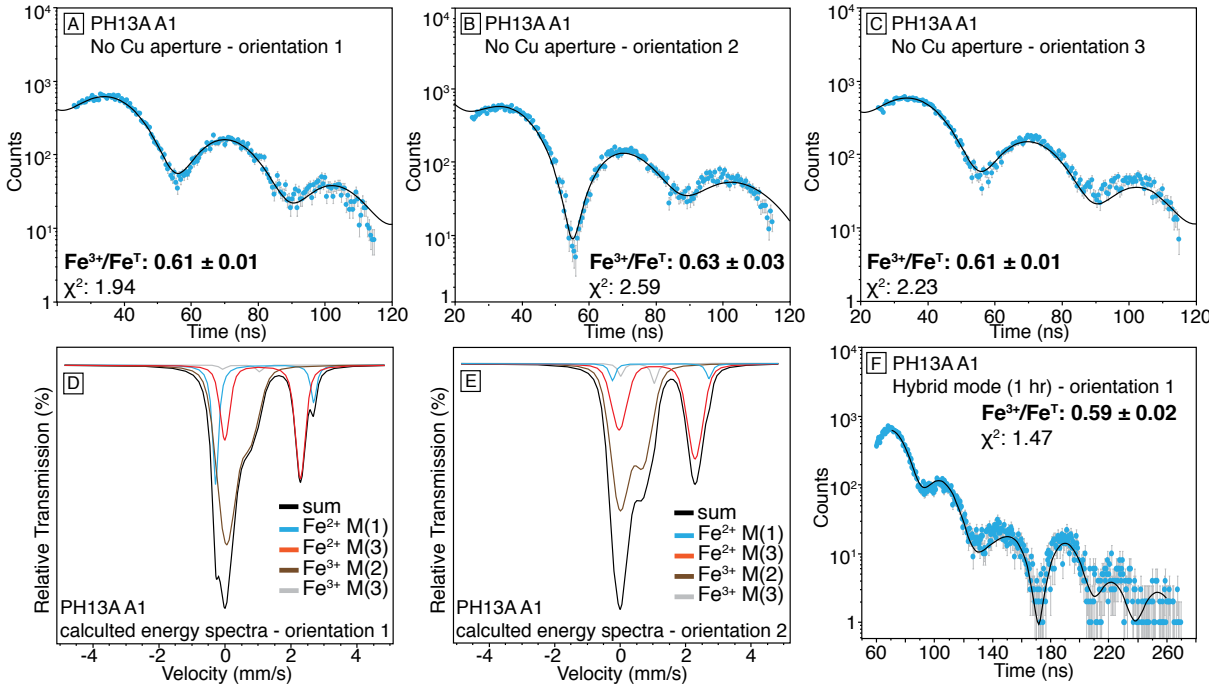

Figure 9. Synchrotron Mössbauer spectra of grain PH13A A1: (**a**, **b**, and **c**) 24-bunch mode spectra of orientation 1, 2, and 3; (**d** and **e**) calculated energy domain data using the best-fit values from **a** and **b**; (**f**) hybrid mode time domain spectrum collected for 1 h for orientation 1. Corresponding best fits are shown with χ^2 for each fit and resulting Fe^{3+}/Fe^{T} ratios. The calculated breakdown of the site doublets and their sum for the expected energy spectra of orientations 1 and 2 uses the best-fit hyperfine parameters, accounts for the transmission integral and the linear polarized nature of the X-rays, and considers a pristine radioactive source width (1 γ). (Color online.)

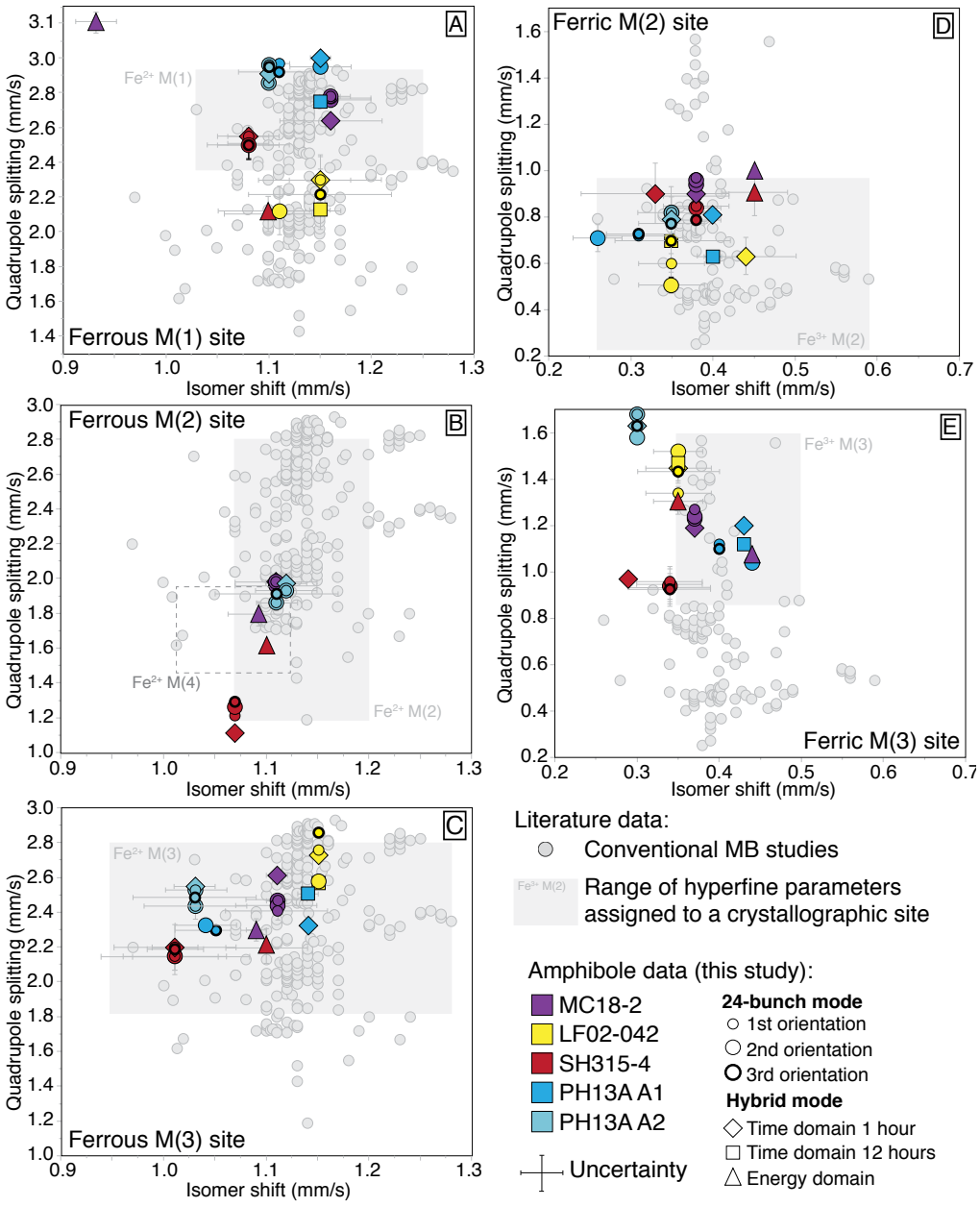

Figure 10. Isomer shift (mm/s) relative to α-iron (corrected for isomer shift between the stainless-steel foils and α-iron) vs. quadrupole splitting (mm/s) for (**a**) ferrous M(1); (**b**) ferrous M(2); (**c**) ferrous M(3); (**d**) ferric M(2); and (**e**) ferric M(3). The gray circles are hyperfine parameters from published conventional Mössbauer studies on amphiboles (data and references in Online Materials[1] Table OM4). The gray boxes in each panel show the range of hyperfine parameters for each site as assigned by conventional Mössbauer studies. The dashed box in B also shows the range in hyperfine parameters for the ferrous M(4) site. Note that literature data are from all amphibole subgroups, not just calcic amphiboles. Uncertainties for the quadrupole splitting and isomer shift determined in this study for Mössbauer sites with weight fractions that are >0.1 are given in Online Materials[1] Table OM1 and shown as vertical and horizontal bars. Uncertainty is not shown if smaller than the symbol size. (Color online.)

oxo-component from ~0.2 to 1.3 apfu correlates with a decrease in the QS of the Fe^{2+} M(1) site (~2.9 to 2.2 mm/s; Fig. 11d).

Identifying SMS spectral signatures of inclusions

Small percentages of a magnetic inclusion, e.g., 2–15% of magnetite, are detectable in the SH315-4 time spectra and energy spectra collected during the hybrid mode. Visually, these are the small-scale high-frequency oscillations in the time spectrum (Fig. 7h) and the additional intensity around 4 mm/s in the energy spectrum (Fig. 7i). Improvements in the fits were achieved by introducing additional sites with texture coefficients close to zero, where one site has magnetic hyperfine parameters consistent with reports for magnetite at ambient conditions (e.g., Glazyrin et al. 2012), but large FWHM values suggesting significant degrees

of non-crystallinity (Online Materials[1] Table OM1).

Iron oxide inclusions can be <10 µm (Fig. 4 and results section) and spectra collected in different orientations without the Cu aperture may not have been collected on exactly the same spot. This explains why a small percentage of magnetite is necessary to fit the hybrid mode but not the 24-bunch mode spectra of grain SH315-4. Similarly, hyperfine parameters and site weights can vary slightly between spectra collected on the same grain in a similar area but not exactly at the same spot. These variations are minimal (Online Materials[1] Table OM1) and can be explained by a spatial deviation of several micrometers.

Discussion

Magmatic vs. dehydrogenated amphiboles

The reddish color, low water content (0.60–0.65 wt%) and heavy hydrogen isotope composition (δD = +2–25‰ relative to SMOW) of grain LF02-042 compared to other grains indicate that it underwent post-crystallization dehydrogenation. The loss of H_2 from the amphibole structure is associated with the oxidation of iron and a shift to heavier H isotope compositions (Fig. 3b). We modeled Rayleigh fractionation of hydrogen isotopes during dehydrogenation of an amphibole crystal. A water content of 1.65 wt% and a δD value of –85‰ was chosen as a starting amphibole composition. This water content is similar to non-dehydrogenated grains analyzed from this sample (unpublished). In addition, this starting δD value is typical for arc magmas determined from melt inclusions (–95 to –12‰; Shaw et al. 2008; Walowski et al. 2015; Fig. 3b). We are able to reproduce the LF02-042 data with a –80‰ to –100‰ fractionation between H_2 vapor and amphibole (Fig. 3b). Amphibole-H_2 vapor fractionation factors are not well constrained experimentally (e.g., Venneman and O'Neil 1996 and references therein), but the values used in the modeling are of the same sign and magnitude as those established by previous experimental studies (between –25 to –200‰; Kuroda et al. 1988). In any case, the high Fe^{3+} content (32–40%) on the M(3) site of sample LF02-042 is interpreted as the result of extensive dehydrogenation and associated oxidation of Fe^{2+} previously occupying this site.

None of the grains have a fully occupied W-site (Cl, F, OH) but contain an oxo-component (O^{2-} on the W-site): SH315-4, 0.54 ± 0.09 apfu; LF02-042, 1.32 ± 0.05 apfu; MC18-2, 0.23 ± 0.12 apfu; PH13A A1, 0.18 ± 0.13 apfu. We interpret the presence of an oxo-component, i.e., a low-volatile content, in SH315-4, MC18-2, and PH13A A1 in combination with arc magmatic hydrogen isotope compositions (Fig. 3b) as reflecting primary crystallization conditions. The oxo-component in these grains can be a result of crystallization under low water activity and/or under very oxidized conditions (i.e., high Fe^{3+}/Fe^{T} in the melt).

Comparison with conventional Mössbauer studies

Figure 10 shows a comparison of QS and IS of amphiboles determined by conventional MB spectroscopy with our results. Identification of peaks and assignment to specific crystallographic sites in conventional MB spectra is hindered by peak

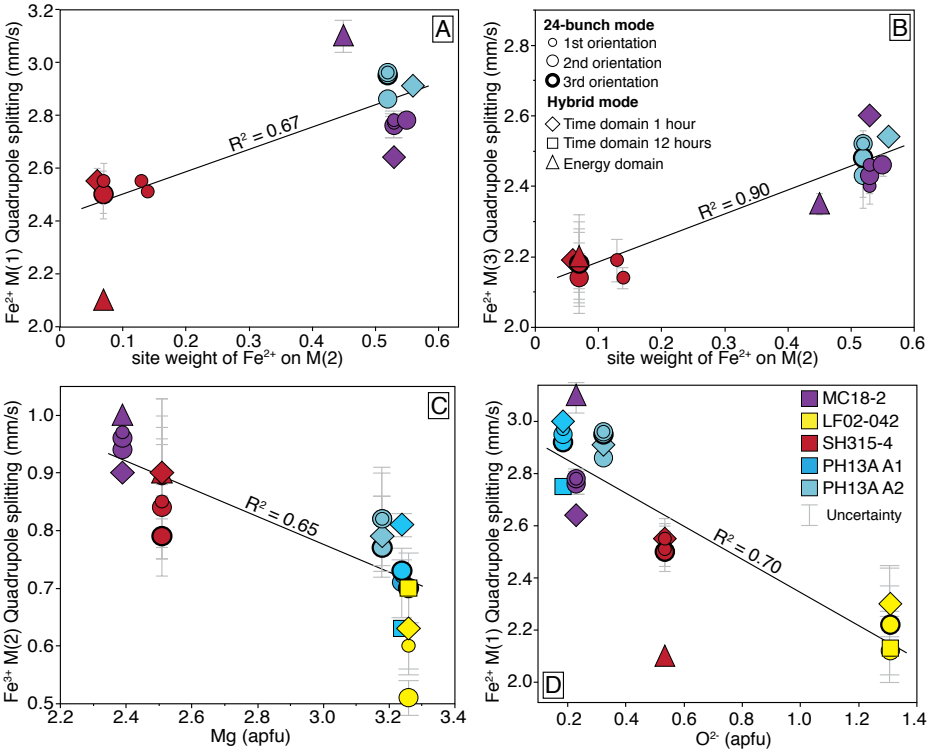

Figure 11. Variations of quadrupole splitting as a function of major element composition, oxo-component, and site occupation: (**a** and **b**) site weight of Fe^{2+} at M(2) vs. quadrupole splitting of Fe^{2+} at the M(1) and M(3) site (mm/s); (**c**) Mg (apfu) vs. quadrupole splitting on the Fe^{3+} M(2) site (mm/s); (**d**) oxo-component (apfu) vs. quadrupole splitting of Fe^{2+} at the M(1) (mm/s). Uncertainties for the quadrupole splitting are given in Online Materials[1] Table OM1. (Color online.)

overlap (e.g., Burns and Greaves 1971). SMS measurements of single crystals permit access to the polarization dependence of the electric field gradient for specific crystallographic sites through the calculation and assignment of Euler angles. Thus, our data provide an opportunity to test previous site assignments.

Both methods generally agree on the range of QS and IS (Fig. 10). However, we find no high IS (>1.2 mm/s; Figs. 10a, 10b, and 10c) for any of the Fe^{2+} sites as suggested by Bancroft and Brown (1975) for hornblende. In general, the QS for the Fe^{2+} sites in conventional MB are assigned based on the assumption of a negative correlation between Fe^{2+} and distortion from the ideal octahedral geometry (Ingalls 1964; Dowty and Lindsley 1973), and the QS is as follows: M(1) > M(3) > M(2) (gray boxes in Fig. 10 show the range of QS and IS for specific crystallographic sites as ascribed by conventional MB). The samples we investigated support this trend, with the exception of grain LF02-042, which shows Fe^{2+} QS of M(3)>M(1) [no Fe^{2+} occupancy on the M(2) site; Figs. 10a and 10c]. We show that LF02-042 is strongly dehydrogenated. Unlike M(2), the M(1) and M(3) sites are adjacent to the O(3) sites in the amphibole structure, which contain OH and can form an oxo-component through the oxidation of Fe on these sites (e.g., Phillips et al. 1989). We thus interpret the QS of M(3) > M(1) for grain LF02-042 as a result of oxidation. This likely causes a decrease of the QS at M(1) due to an increased distortion of this site. A full structure refinement is necessary to fully verify this. Oxidation of Fe^{2+} at M(1) and an associated decrease in QS during dehydrogenation in a riebeckite amphibole structure has also been shown by Oberti et al. (2018).

The results of the Euler angle calculations show that the angles of the M(1) and M(2) sites are very similar (Online Materials[1] Table OM3). Thus, the distinguishing feature of these sites is the difference in QS both for Fe^{2+} and Fe^{3+}. This is in agreement with conventional MB studies, which generally assign M(2) a smaller QS (Fig. 10b) compared to the M(1) site (Fig. 10a) based on lattice distortion (e.g., Hawthorne 1983).

Charge-balance calculations allow one to estimate the amount of Fe^{2+} on the M(4) site if the water content of the amphibole is known. For amphiboles investigated in this study, we are able to calculate the amount of Fe^{2+} on the M(4) using charge balance and the water content determined by SIMS. Ferrous iron varies from 0.02 to 0.11 apfu on the M(4) site. We note that introducing a Fe^{2+} M(4) site in our model does not improve the fitting of our spectra, which is supported by charge balance considerations suggesting Fe^{2+} only occurs in small quantities on the M(4) site (≤0.11 apfu) in our samples. Previous studies using conventional MB (e.g., Goldman 1979; Iezzi et al. 2003; Driscall et al. 2005), however, indicate the presence of Fe^{2+} at the M(4) site. We do not find strong evidence for this in the present study based on our fitting models. A full structural refinement would clarify the magnitude of Fe^{2+} on the M(4) site.

Energy-domain spectra collected with our new setup allows a comparison to conventional MB energy-domain spectra. We compare sample MC18-2 to two calcic amphibole conventional MB spectra comprising similar Fe^{3+}/Fe^{T} ratios: 0.25 (sample BCc-13; Bancroft and Brown 1975; FeO: 17.09 wt%) and 0.17 (sample A2; Schmidbauer et al. 2000; FeO: 21.01 wt%). All spectra (MC18-2 and published spectra) consist of one doublet with broad lines due to the dominance of Fe^{2+}. An additional weak component ("shoulder") occurs due to Fe^{3+}. Published amphibole spectra are fitted with 4 sites: three Fe^{2+} and one Fe^{3+}. While Bancroft and Brown (1975) ascribe Fe^{2+} to different crystallographic sites according to decreasing QS [M(1) > M(3) > M(2)], Schmidbauer et al. (2000) ascribed the smallest ferrous QS (1.91 mm/s) to M(3). Our spectra, on the other hand, are fitted with five sites (three Fe^{2+} and two Fe^{3+}) and ferrous QS decrease similarly from M(1) to M(3) and M(2). While general ranges in QS and IS are similar between our study and published fits, the presence of an additional Fe^{3+} site in our data is justified due to the fact that we consider both the energy and time domain of multiple orientations to arrive at the best model to explain the hyperfine parameters. This approach had never been done before this study. We further calculated energy domain spectra from time domain spectra for 24-bunch mode data of sample PH13A A1 for orientation 1 and 2 (Figs. 9d and 9e). These allow a direct comparison of orientation effects. However, analysis of the same amphibole grain with SMS and conventional MB is necessary to fully compare fitting results by both methods.

Variation of hyperfine parameters with composition

Previous studies, using a combination of conventional MB spectroscopy and XRD, detected correlations between QS and IS of Fe^{3+} and Fe^{2+} and the chemical composition of amphibole grains. Redhammer and Roth (2002) observed an increase in QS of Fe^{2+} at M(1) and M(3) with an increase in the average ionic radius of the M(2) site. In our study, the average ionic radius of the M(2) site cannot be determined without a full structure refinement. However, we can use the site weight of Fe^{2+} at M(2) as a rough proxy for the average ionic radius, as it has the largest radius (0.78 Å in octahedral coordination) of all cations potentially occupying this site (Mg^{2+}: 0.72 Å; Fe^{3+}: 0.65 Å; Al^{3+}: 0.53 Å; Ti^{4+}: 0.60 Å). We observe an increase in QS at M(1) and M(3) with an increase in Fe^{2+} occupancy at the M(2) site (Figs. 11a and 11b). Lower site weights of Fe^{2+} at M(2) indicate the substitution with other cations, which would cause a distortion at this site resulting in lower Fe^{2+} QS.

Mg^{2+}–Fe^{2+} substitution in amphibole is common, and the $Mg/(Mg+Fe^{2+})$ ratio has been used for nomenclature purposes (e.g., Leake et al. 2004). We observe an increase in Mg (2.4 to 3.2 apfu) at the C-site accompanied by a decrease of QS on the Fe^{3+} M(2) site from ~0.9 to 0.6 mm/s (Fig. 11c). On the contrary, Della Ventura et al. (2016) observed an increase in QS of Fe^{3+} at M(2) with increasing Mg in richterite. Given the known positive correlation between Fe^{3+} QS and the electronic distortion at the octahedral site (e.g., Della Ventura et al. 2016), this trend can be interpreted as a decrease in distortion by the substitution of Mg. QS of the Fe^{2+} sites and IS of all sites do not show a systematic dependence with Mg concentration.

We observe a decrease in QS of Fe^{2+} at M(1) with increasing oxo-component (Fig. 11d). The formation of an oxo-component is accompanied by shortening of the M-O(3) bond lengths and thus causes an increase in the site distortion, which is reflected in lower QS at the Fe^{2+} M(1) site. There appears to be no systematic change in the QS or IS of the other Fe^{2+} sites.

Ferric iron accommodation

Three mechanisms have been proposed to accommodate Fe^{3+} in the amphibole structure (Clowe et al. 1988; Popp et al. 1990; Dyar et al. 1993; King et al. 2000; Oberti et al. 2007):

Oxo-component creation:

$$Fe^{2+}_{C\text{-site}} + OH^{-}_{W\text{-site}} = Fe^{3+}_{C\text{-site}} + O^{2-}_{W\text{-site}} + \square_{H^+} \quad (1)$$

Substitution on the octahedral site:

$$Al^{3+}_{C\text{-site}} = Fe^{3+}_{C\text{-site}} \quad (2)$$

A-site vacancy creation:

$$(Na,K)^{+}_{A\text{-site}} + Fe^{2+}_{C\text{-site}} = \square_{A\text{-site}} + Fe^{3+}_{C\text{-site}} \quad (3)$$

Figure 12 illustrates these accommodation mechanisms with data from this study and a literature compilation of studies determining amphibole major element compositions, Fe^{3+}/Fe^{T} ratios, and water content (Online Materials[1] Table OM6 lists the data, references, and the method by which data was acquired). No single mechanism can univocally explain Fe^{3+} accommodation in our samples and the literature data. Mechanism 1 appears to be an important process to accommodate Fe^{3+} in LF02-042 and PH13A A2 (and potentially MC18-2 given its proximity to the 1:1 line). However, incorporation of Ti^{4+} can also locally balance the oxo-component (e.g., Oberti et al. 2007; Fig. 12b). The

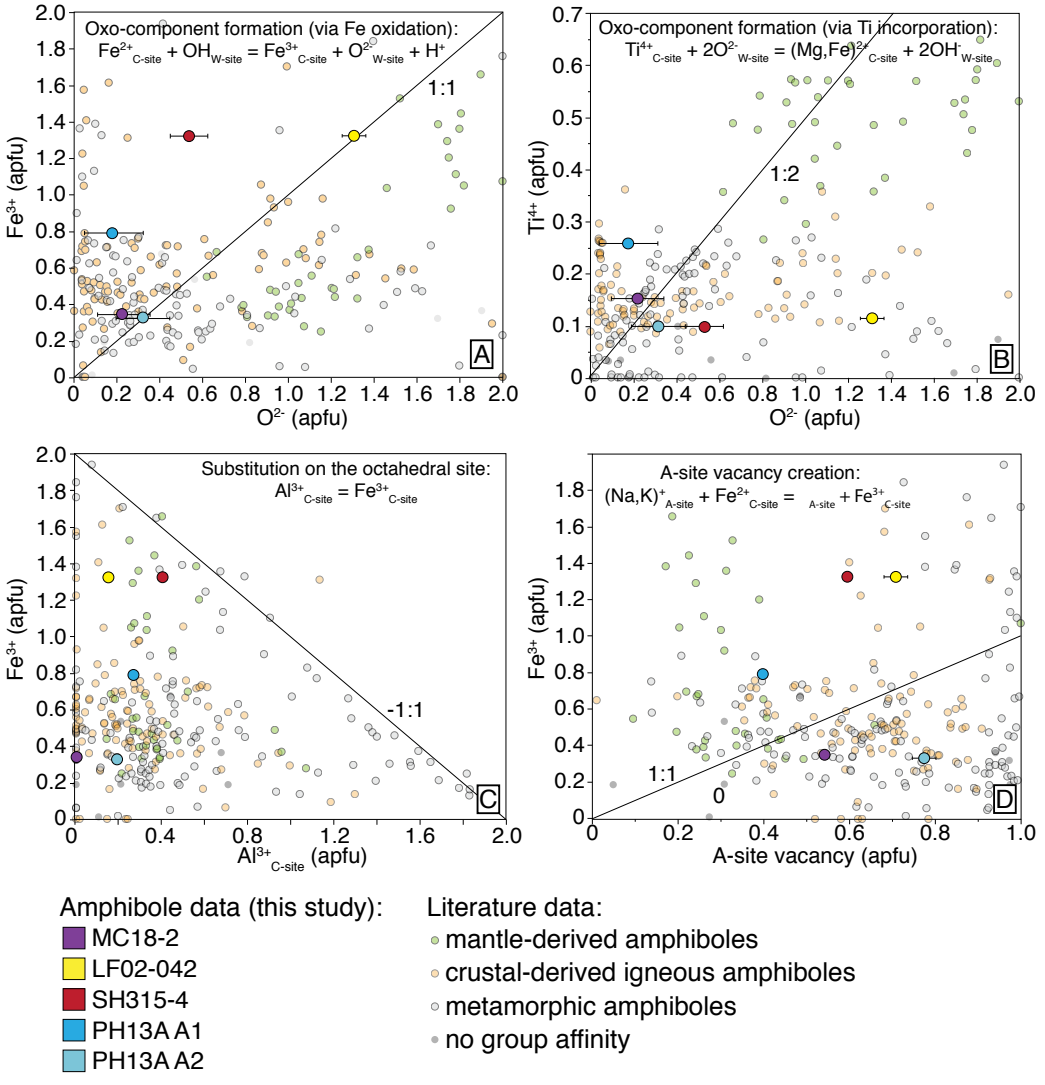

Figure 12. Different mechanisms of ferric iron and oxo-component accommodation in the amphibole structure. Ferric iron determined by synchrotron Mössbauer spectroscPopy from area on the grain where major element composition and water content was also determined. The oxo-component was calculated from water contents determined by secondary-ion mass spectrometry. In addition, literature data are shown (Online Materials[1] Table OM6 lists the data, references, and the various methods used to determine major element compositions, Fe^{3+}/Fe^{T} ratios, and water content). Mantle-derived amphiboles include ultramafic associations and megacrysts from basaltic lavas; crustal-derived igneous amphiboles encompass amphiboles derived from plutonic and volcanic lithologies; metamorphic amphiboles encompass various metamorphic facies and lithological compositions. Amphibole formula calculations after Locock (2014). (**a**) An oxo-component (apfu) vs. ferric iron (apfu); (**b**) oxo-component (apfu) vs. titanium on the C-site (apfu); (**c**) aluminum on the C-site (apfu) vs. ferric iron (apfu); (**d**) A-site vacancy (apfu) vs. ferric iron (apfu). Error bar is smaller than the symbol size if not shown. (Color online.)

literature data shows that both mechanisms are likely important in mantle-derived amphiboles (see also King et al. 1999; Oberti et al. 2007). In grains LF02-042, MC18-2, and PH13A A2, the oxo-component (1.32 ± 0.05, 0.23 ± 0.12, and 0.32 ± 0.12 apfu) can account for all of the Fe^{3+} (1.29, 0.35, and 0.32 apfu; calculated from EMPA and SMS data) within uncertainty. The difference in the hydrogen isotope compositions of LF02-042 and MC18-2 indicates that the oxo-component in grain MC18-2 is not a consequence of dehydrogenation but might be a result of crystallization under reduced conditions and/or from a melt with low-water activity. For grains SH315-4 and PH13A A1, all three mechanisms are required to accommodate the Fe^{3+} content (1.22 and 0.74 apfu). The oxo-component (0.54 ± 0.09 and 0.18 ± 0.13 apfu) alone cannot accommodate the amount of Fe^{3+} (even if iron oxidation is the sole charge-balance mechanism). In addition to the oxo-component, a combination of A-site vacancies and substitution of Fe^{3+} for Al^{3+} on the C-site is required (Figs. 12c and 12d). As both grains do not show signs of post-crystallization dehydrogenation, we conclude that the combination of all accommodation mechanisms occurred during crystallization and was controlled by crystallization pressure (Al incorporation into the amphibole), water activity in the melt (oxo-component), and melt composition (Na and K content).

The literature data shown in Figure 12 do not reveal a clear dominance of one Fe^{3+} accommodation mechanism. We speculate here that this may be due to: (1) bulk techniques averaging intra-grain compositional heterogeneities and inclusions (e.g., biotite); (2) different amphibole groups favor different accommodation mechanisms depending on their composition (e.g., mantle-derived amphiboles, Figs. 12a and 12b); (3) that several accommodation mechanisms are required to account for all Fe^{3+}; and (4) individual grains have been variably affected by dehydrogenation. Therefore, experimental amphiboles synthesized under controlled conditions are the best candidates to understand ferric iron accommodation mechanisms.

Intra-grain heterogeneities in Fe^{3+}/Fe^{T} ratios

Igneous amphiboles commonly show intra-grain zonation in major and trace elements, often used to infer magmatic processes (e.g., Barnes et al. 2016; Kiss et al. 2014). Thus, it is reasonable to assume that Fe^{3+}/Fe^{T} ratios vary within single grains, recording changes in crystallization conditions and/or post-crystallization oxidation. The high spatial resolution of SMS allows detecting these variations.

Two areas on grain SH315-4 were analyzed: the center of the grain (Fig. 4c) yielded Fe^{3+}/Fe^{T} ratios of 0.59 ± 0.02 to 0.63 ± 0.02, generally higher than two spots close to the edge (spots 2 and 3; 0.51 ± 0.02 and 0.59 ± 0.02, respectively; Fig. 4c). Attempts to fit spectra from both areas with the same model failed; instead, lower Fe^{3+}/Fe^{T} ratios for spots 2 and 3 compared to the area in the center were required indicating intra-grain heterogeneity in Fe^{3+}/Fe^{T} ratios. In combination with the major element data, this could be related to magmatic or post-eruption processes. For example, dacites from the June 1991 eruption of Mt. Pinatubo contain amphibole phenocrysts with cores rich in Al_2O_3 and TiO_2 (e.g., Bernard et al. 1996; Scaillet and Evans 1999; Fig. 4d), either due to an early mixing event or a higher-pressure crystallization stage prior to eruption (Prouteau and Scaillet 2003; Scaillet and Evans 1999). Grain PH13A A1 represents an example of a high-Al_2O_3 core, whereas grain PH13A A2 exemplifies a rim or low-Al_2O_3 phenocryst. Although not analyzed in the same grain, SMS is able to capture a difference in Fe^{3+}/Fe^{T} ratios between high-Al_2O_3 cores with 0.62 ± 0.01 (PH13A A1) and low-Al_2O_3 rims/phenocrysts with 0.20 ± 0.01 (PH13A A2).

A comparison of our data with those of Underwood et al. (2012, 2013) shows the importance of a high spatial resolution technique such as SMS to distinguish intra-grain compositional heterogeneities and avoid the analysis of inclusions. Underwood et al. analyzed amphibole grains from samples LF02-042 and SH315-4, using wet chemistry on aliquots of multiple grains. Their analyses yielded for LF02-042: Fe^{3+}/Fe^{T}: 0.56, H_2O: 2.3 wt%, δD: –68 ‰, and for SH315-4: Fe^{3+}/Fe^{T}: 0.99, H_2O: 1.7 wt%, δD: –86 ‰ significantly different from the values obtained in our study. It is likely that the samples contain mixed crystal populations (e.g., with grains with different degrees of dehydrogenation) such that the results from our and their studies cannot be directly related. However, the elevated water contents of 2.3 wt% measured by Underwood et al. (2012) in LF02-042 may suggest the analysis of amphibole with biotite inclusions, which are abundant in this sample.

A mixed analysis of amphibole and biotite, multiple crystal populations (as in the case of PH13A A1) as well as iron oxides would yield higher Fe^{3+}/Fe^{T} ratios than the amphibole alone. We demonstrated this with SMS energy- and time-domain spectra collected for SH315-4 that exhibited signatures from an inclusion characterized by magnetic ordering (see results section).

Comparison with other methods determining Fe^{3+}/Fe^{T} ratios in amphibole

Other methods have been used to determine the Fe^{3+}/Fe^{T} ratios in amphibole with a similar high spatial resolution. The most common applied are X-ray absorption near edge structure spectroscopy [XANES; e.g., Dyar et al. (2016)] and EMPA (e.g., Li et al. 2019), which use spot sizes of 7 × 9 µm [Dyar et al. (2016); but spots sizes of ~2–5 μm^2 are possible and applied to glass analyses; McCanta et al. (2017)] and 20 × 20 µm (e.g., Li et al. 2019), respectively. While X-ray photoelectron spectroscopy (XPS) (e.g., Fantauzzi et al. 2010) and electron energy-loss spectroscopy (EELS) have been used to analyze surface Fe^{3+}/Fe^{T} ratios, the latter has been shown to probe the nanometer scale (e.g., Garvie and Busek 1998). Other methods, such as the Mössbauer milliprobe, allow the analyses of small sample sizes (as small as ~50 µm; McCammon 1994), however, this method has not been applied to amphiboles. XANES, EMPA, EELS, and XPS require the use of reference material for data interpretation. Dyar et al. (2002), for example, used fayalite, magnetite, hematite, and aegirine with known Fe^{3+}/Fe^{T} ratios determined by conventional MB spectroscopy and/or wet chemistry to study amphiboles using XANES. No well-characterized reference material exists for calcic amphibole. SMS and other Mössbauer setups (e.g., Mössbauer millioprobe) do not require reference spectra, therefore eliminating dependency on accuracy of reference material values. Other advantages of SMS over conventional MB spectroscopy are a linear polarization of the source and shorter data collection time on natural amphiboles

(samples not enriched with ^{57}Fe). The conventional MB source emits unpolarized radiation, which significantly reduces the spectral sensitivity to electric-field-gradient tensor orientation in single crystals. While conventional MB spectroscopy requires multiple-day data collection, the spectra in this study were obtained in 1 to 12 h. Finally, the ability to measure both energy spectra (with a polarized source) and time spectra (with an extended time window) at the same micrometer-sized spot offers a notable advantage over conventional MB spectroscopy, especially when measuring samples containing multivalent iron and with multiple sites, as was done here.

Beam-induced iron oxidation was documented in hydrous glass using XANES [synchrotron radiation; Cottrell et al. (2018)] and in amphibole using EMPA [electron beam; Li et al. (2019)]. Beam-induced damage is not only a function of beam power density (flux density) but also of sample thickness and composition (e.g., water content) and the accumulated dose (i.e., flux times exposure time). During our SMS analyses, the flux density was 1.7×10^7 and 1.0×10^{10} photons/s/μm^2 during the 24-bunch mode and the hybrid time mode, respectively. The flux during the collection of the energy domain spectra was negligible because the incident bandwidth on the sample was very small (10^{-8} eV). Cottrell et al. (2018) argued that at a flux of $\leq 6 \times 10^7$ photons/s/μm^2 the oxidation effect is negligible. This flux is higher than the one used during our 24-bunch mode experiments; however, the results by Cottrell et al. (2018) cannot be directly compared to our data as the composition, structure, thickness, and water content of our samples are different. XANES studies of amphiboles by Bajt et al. (1994), Delaney et al. (1998), and Dyar et al. (2002, 2016) do not provide information regarding beam flux during data collection, nor did they consider beam-induced iron oxidation. However, the agreement between XANES and conventional MB and/or wet chemistry results in these past studies suggests that beam-induced oxidation is minimal. The fact that we have been able to fit the hybrid mode and 24-bunch mode spectra with very similar models supports the notion that beam-induced oxidation can be neglected in the current study. We also analyzed grain PH13A A1 twice for water content in the same area: before and after SMS data collection. The data shows no difference before (1.72 ± 0.14 wt%) and after (1.79 ± 0.13 wt%; an average of three analyses) SMS data collection. However, a more detailed and systematic study assessing beam-damage study should be undertaken.

Implications

The workflow presented in this study combining multiple high spatial resolution techniques (EMPA, SIMS, and SMS) on the same area of individual amphibole grains allows distinguishing between post-crystallization and crystallization effects of Fe oxidation. This is crucial if analyzed Fe^{3+}/Fe^{T} ratios are to be used to infer the conditions during amphibole formation. Natural igneous amphiboles erupted in arc volcanoes, for example, can show intra-grain compositional zonation [e.g., Gorbach et al. (2020)], which can reflect distinct crystallization conditions and levels in a vertically extensive magma plumbing system (e.g., Humphreys et al. 2019). Resolving these conditions is crucial for an understanding of the evolution of magmatic systems. In particular, variations in the Fe^{3+}/Fe^{T} ratios in a melt can be recorded by the Fe^{3+}/Fe^{T} ratios in amphiboles during crystallization (e.g., King et al. 2000). The high spatial resolution and relatively low uncertainties of the SMS analysis allow for the detection of small variations in Fe^{3+}/Fe^{T} ratios within individual grains, and in combination with results from EMPA and SIMS these can be attributed to changing crystallization conditions or the effects of post-crystallization oxidation. Future work should use electron backscatter diffraction to determine the lattice orientation of amphiboles in thick sections; this will allow SMS analysis in a textural context.

Furthermore, SMS distinguishes between specific crystallographic sites in the amphibole structure occupied by Fe^{2+} and Fe^{3+}. In combination with other methods, such as infrared spectroscopy and XRD, SMS is a promising avenue to improve our understanding of the structural changes in amphibole accompanying dehydrogenation and the general long-range order of iron as a function of mineral chemistry.

Acknowledgments

The authors thank Yunbin Guo (Caltech), Larry Henling (Caltech), and Chi Ma (Caltech) for assistance with SIMS, XRD, and EMPA analyses, respectively. Johannes Buchen, Vasilije Dobrosavljevic, Olivia Pardo, Mary Peterson, and Emma Sosa (all Caltech) helped during in-person and remote beamtime at Argonne National Laboratory. Sandy Underwood (Montana State University), Carl Thornber (USGS), and Kevin Schrecengost (UC Davis) shared sample material, which made this study possible. We also thank Darby Dyar, David Jenkins, and an anonymous reviewer for their helpful and constructive reviews, which improved this manuscript.

Funding

This work was supported by NSF grant 1841790 to C.E. Bucholz and J.M. Jackson. This research used resources of the Advanced Photon Source, a U.S. Department of Energy (DOE) Office of Science User Facility operated for the DOE Office of Science by Argonne National Laboratory under Contract No. DE-AC02-06CH11357.

References cited

Abdu, Y.A., and Hawthorne, F.C. (2009) Crystal structure and Mössbauer spectroscopy of tschermakite from the ruby locality at Fiskenaesset, Greenland. Canadian Mineralogist, 47, 917–926.

Armstrong, J.T. (1995) CITZAF-a package of correction programs for the quantitative electron microbeam X-ray-analysis of thick polished materials, thin-films, and particles. Microbeam Analysis, 4, 177–200.

Bajt, S., Sutton, S., and Delaney, J. (1994) X-ray microprobe analysis of iron oxidation states in silicates and oxides using X-ray absorption near edge structure (XANES). Geochimica et Cosmochimica Acta, 58, 5209–5214.

Bancroft, G.M., and Burns, G.R. (1969) Mössbauer and absorption spectral study of alkali amphiboles. Mineralogical Society of America Special Paper, 2, 137–148.

——— (1975) A Mössbauer study of coexisting hornblendes and biotites: Quantitative Fe^{3+}/Fe^{2+} ratios. American Mineralogist, 60, 265–272.

Barnes, C.G., Memeti, V., and Coint, N. (2016) Deciphering magmatic processes in calc-alkaline plutons using trace element zoning in hornblende. American Mineralogist, 101, 328–342.

Bernard, A., Knittel, U., Weber, B., Weis, D., Albrecht, A., Hattori, K., Klein, J., and Oles, D. (1996) Petrology and geochemistry of the 1991 eruption products of Mount Pinatubo. Fire and mud: Eruptions and lahars of Mount Pinatubo (Luzon, Philippines), 767–797.

Boyce, J.W., Liu, Y., Rossman, G.R., Guan, Y., Eiler, J.M., Stolper, E.M., and Taylor, L.A. (2010) Lunar apatite with terrestrial volatile abundances. Nature, 466, 466–469.

Bruker (2012a) APEX3. Bruker AXS inc., Madison, Wisconsin, U.S.A.

——— (2012b) CELL_NOW. Bruker AXS inc., Madison, Wisconsin, U.S.A.

Burns, R.G., and Greaves, C. (1971) Correlations of infrared and Mössbauer site population measurements of actinolites. American Mineralogist, 56, 2010–2033.

Chin, E.J., Soustelle, V., Hirth, G., Saal, A.E., Kruckenberg, S.C., and Eiler, J.M. (2016) Microstructural and geochemical constraints on the evolution of deep arc lithosphere. Geochemistry, Geophysics, Geosystems, 17, 2497–2521.

Clowe, C.A., Popp, R.K., and Fritz, S.J. (1988) Experimental investigation of the effect of oxygen fugacity on ferric-ferrous ratios and unit-cell parameters of four natural clinoamphiboles. American Mineralogist, 73, 487–499.

Clynne, M.A., and Muffler, L.J.P. (2010) Geologic map of Lassen Volcanic

National Park and vicinity, California. US. Department of the Interior, U.S. Geological Survey.
Cottrell, E., Lanzirotti, A., Mysen, B., Birner, S., Kelley, K.A., Botcharnikov, R., Davis, F.A., and Newville, M. (2018) A Mössbauer-based XANES calibration for hydrous basalt glasses reveals radiation-induced oxidation of Fe. American Mineralogist, 103, 489–501.
Crowley, J., Schoene, B., and Bowring, S. (2007) U-Pb dating of zircon in the Bishop Tuff at the millennial scale. Geology, 35, 1123–1126.
Dauphas, N., Roskosz, M., Alp, E.E., Golden, D.C., Sio, C.K., Tissot, F.L.H., Hu, M.Y., Zhao, J., Gao, L., and Morris, R.V. (2012) A general moment NRIXS approach to the determination of equilibrium Fe isotopic fractionation factors: application to goethite and jarosite. Geochimica et Cosmochimica Acta, 94, 254–275.
Delaney, J.S., Dyar, M.D., Sutton, S.R., and Bajt, S. (1998) Redox ratios with relevant resolution: Solving an old problem by using the synchrotron micro-XANES probe. Geology, 26, 139–142.
Della Ventura, G., Redhammer, G.J., Iezzi, G., Hawthorne, F.C., Papin, A., and Robert, J.-L. (2005) A Mössbauer and FTIR study of synthetic amphiboles along the magnesioriebeckite–ferri-clinoholmquistite join. Physics and Chemistry of Minerals, 32, 103–113.
Della Ventura, G., Redhammer, G.J., Robert, J.-L., Sergent, J., Iezzi, G., and Cavallo, A. (2016) Crystal-chemistry of synthetic amphiboles along the richterite–ferro-richterite join: A combined spectroscopic (FTIR, Mössbauer), XRD, and microchemical study. Canadian Mineralogist, 54, 97–114.
Della Ventura, G., Mihailova, B., Susta, U., Cestelli Guidi, M., Marcelli, A., Schlüter, J., and Oberti, R. (2018) The dynamics of Fe oxidation in riebeckite: A model for amphiboles. American Mineralogist, 103, 1103–1111.
Deloule, E., France-Lanord, C., and Albarede, F, and (1991) D/H analysis of minerals by ion probe. Stable Isotope Geochemistry: A Tribute to Samuel Epstein, 3, 53–62.
Dowty, E., and Lindsley, D. (1973) Mössbauer spectra of synthetic hedenbergite-ferrosilite pyroxenes. American Mineralogist, 58, 850–868.
Driscall, J., Jenkins, D.M., Dyar, M.D., and Bozhilov, K.N. (2005) Cation ordering in synthetic low-calcium actinolite. American Mineralogist, 90, 900–911.
Dyar, M.D., Mackwell, S.J., McGuire, A.V., Cross, L.R., and Robertson, J.D. (1993) Crystal chemistry of Fe^{3+} and H^{+} in mantle kaersutite: Implications for mantle metasomatism. American Mineralogist, 78, 968–979.
Dyar, M.D., Lowe, E.W., Guidotti, C.V., and Delaney, J.S. (2002) Fe^{3+} and Fe^{2+} partitioning among silicates in metapelites: A synchrotron micro-XANES study. American Mineralogist, 87, 514–522.
Dyar, M.D., Agresti, D.G., Schaefer, M.W., Grant, C.A., and Sklute, E.C. (2006) Mössbauer spectroscopy of Earth and planetary materials. Annual Review of Earth and Planetary Sciences, 34, 83–125.
Dyar, M.D., Breves, E.A., Gunter, M.E., Lanzirotti, A., Tucker, J.M., Carey, C.J., Peel, S.E., Brown, E.B., Oberti, R., Lerotic, M., and Delaney, J.S. (2016) Use of multivariate analysis for synchrotron micro-XANES analysis of iron valence state in amphiboles. American Mineralogist, 101, 1171–1189.
Ernst, W., and Wai, C. (1970) Mössbauer, infrared, X-ray and optical study of cation ordering and dehydrogenation in natural and heat-treated sodic amphiboles. American Mineralogist, 55, 1226–1258.
Fantauzzi, M., Pacella, A., Atzei, D., Gianfagna, A., Andreozzi, G.B., and Rossi, A. (2010) Combined use of X-ray photoelectron and Mössbauer spectroscopic techniques in the analytical characterization of iron oxidation state in amphibole asbestos. Analytical and Bioanalytical Chemistry, 396, 2889–2898.
Fultz, B. (2002) Mössbauer spectrometry. Characterization of Materials, 1–21.
Garvie, L.A., and Buseck, P.R. (1998) Ratios of ferrous to ferric iron from nanometre-sized areas in minerals. Nature, 396(6712), 667–670.
Glazyrin, K., McCammon, C., Dubrovinsky, L., Merlini, M., Schollenbruch, K., Woodland, A., and Hanfland, M. (2012) Effect of high pressure on the crystal structure and electronic properties of magnetite below 25 GPa. American Mineralogist, 97, 128–133.
Goldman, D.S. (1979) A reevaluation of the Mössbauer spectroscopy of calcic amphiboles. American Mineralogist, 64, 109–118.
Goldman, D.S., and Rossman, G.R. (1977) The identification of Fe^{2+} in the *M*(4) site of calcic amphiboles. American Mineralogist, 62, 205–216.
Gorbach, N., Philosofova, T., and Portnyagin, M. (2020) Amphibole record of the 1964 plinian and following dome-forming eruptions of Shiveluch volcano, Kamchatka. Journal of Volcanology and Geothermal Research, 407, 107108.
Hawthorne, F. (1983) Quantitative characterization of site-occupancies in minerals. American Mineralogist, 68, 287–306.
Hawthorne, F.C., and Oberti, R. (2007) Amphiboles: Crystal chemistry. Reviews in Mineralogy and Geochemistry, 67, 1, 1–54.
Hawthorne, F.C., Oberti, R., Harlow, G.E., Maresch, W.V., Martin, R.F., Schumacher, J.C., and Welch, M.D. (2012) Nomenclature of the amphibole supergroup. American Mineralogist, 97, 2031–2048.
Hildreth, W. (2004) Volcanological perspectives on Long Valley, Mammoth Mountain, and Mono Craters: Several contiguous but discrete systems. Journal of Volcanology and Geothermal Research, 136, 169–198.
Hildreth, W., and Mahood, G.A. (1986) Ring-fracture eruption of the Bishop Tuff. Geological Society of America Bulletin, 97, 396–403.
Humphreys, M.C., Cooper, G.F., Zhang, J., Loewen, M., Kent, A.J., Macpherson, C.G., and Davidson, J.P. (2019) Unravelling the complexity of magma plumbing at Mount St. Helens: A new trace element partitioning scheme for amphibole. Contributions to Mineralogy and Petrology, 174, 9.
Iezzi, G., Della Ventura, G., Pedrazzi, G., Robert, J.L., and Oberti, R. (2003) Synthesis and characterisation of ferri-clinoferroholmquistite, $\square Li_2(Fe^{2+}_3Fe^{3+}_2)Si_8O_{22}(OH)_2$. European Journal of Mineralogy, 15, 321–327.
Ingalls, R. (1964) Electric-field gradient tensor in ferrous compounds. Physical Review, 133, A787 –A795.
Jackson, J.M., Hamecher, E.A., and Sturhahn, W. (2009) Nuclear resonant X-ray spectroscopy of (Mg,Fe)SiO_3 orthoenstatites. European Journal of Mineralogy, 21, 551–560.
Johnson, M.C., and Rutherford, M.J. (1989) Experimental calibration of the aluminum-in-hornblende geobarometer with application to Long Valley caldera (California) volcanic rocks. Geology, 17, 837–841.
King, P.L., Hervig, R.L., Holloway, J.R., Vennemann, T.W., and Righter, K. (1999) Oxy-substitution and dehydrogenation in mantle-derived amphibole megacrysts. Geochimica et Cosmochimica Acta, 63, 3635–3651.
King, P., Hervig, R., Holloway, J., Delaney, J., and Dyar, M. (2000) Partitioning of Fe^{3+}/Fe^{total} between amphibole and basanitic melt as a function of oxygen fugacity. Earth and Planetary Science Letters, 178, 97–112.
Kiss, B., Harangi, S., Ntaflos, T., Mason, P.R., and Pál-Molnár, E. (2014) Amphibole perspective to unravel pre-eruptive processes and conditions in volcanic plumbing systems beneath intermediate arc volcanoes: a case study from Ciomadul volcano (SE Carpathians). Contributions to Mineralogy and Petrology, 167, 986.
Krawczynski, M.J., Grove, T.L., and Behrens, H. (2012) Amphibole stability in primitive arc magmas: effects of temperature, H_2O content, and oxygen fugacity. Contributions to Mineralogy and Petrology, 164, 317–339.
Kuroda, Y., Matsuo, S., and Yamada, T. (1988) D/H fractionation during dehydration of hornblende, mica and volcanic glass. Journal of Mineralogy, Petrology and Economic Geology, 83(3), 85–94.
Leake, B.E., Woolley, A.R., Birch, W.D., Burke, E.A.J., Ferraris, G., Grice, J.D., Hawthorne, F.C., Kisch, H.J., Krivovichev, V.G., Schumacher, J.C., Stephenson, N.C.N., and Whittaker, E.J.W. (2004) Nomenclature of amphiboles: Additions and revisions to the International Mineralogical Association's amphibole nomenclature. Mineralogical Magazine, 68, 209–215.
Li, X., Zhang, C., Almeev, R.R., Zhang, X.-C., Zhao, X.-F., Wang, L.-X., Koepke, J., and Holtz, F. (2019) Electron probe microanalysis of $Fe^{2+}/\Sigma Fe$ ratios in calcic and sodic-calcic amphibole and biotite using the flank method. Chemical Geology, 509, 152–162.
Locock, A.J. (2014) An Excel spreadsheet to classify chemical analyses of amphiboles following the IMA 2012 recommendations. Computers & Geosciences, 62, 1–11.
Makino, K., and Tomita, K. (1989) Cation distribution in the octahedral sites of hornblendes. American Mineralogist, 74, 1097–1105.
Margulies, S., and Ehrman, J.R. (1961) Transmission and line broadening of resonance radiation incident on a resonant absorber. Nuclear Instruments and Methods, 12, 131–137.
McCammon, C.A. (1994) A Mössbauer milliprobe: Practical considerations. Hyperfine Interactions, 92, 1235–1239.
McCanta, M.C., Dyar, M.D., Rutherford, M.J., Lanzirotti, A., Sutton, S.R., and Thomson, B.J. (2017) In situ measurement of ferric iron in lunar glass beads using Fe-XAS. Icarus, 285, 95–102.
Miyagi, I., Matsubaya, O., and Nakashima, S. (1998) Change in D/H ratio, water content and color during dehydration of hornblende. Geochemical Journal, 32, 33–48.
Morrison, R.A., Jackson, J.M., Sturhahn, W., Zhao, J., and Toellner, T.S. (2019) High-pressure thermoelasticity and sound velocities of Fe-Ni-Si alloys. Physics of the Earth and Planetary Interiors, 294, 106268.
Mosenfelder, J.L., Le Voyer, M., Rossman, G.R., Guan, Y., Bell, D.R., Asimow, P.D., and Eiler, J.M. (2011) Analysis of hydrogen in olivine by SIMS: Evaluation of standards and protocol. American Mineralogist, 96, 1725–1741.
Murphy, C.A., Jackson, J.M., and Sturhahn, W. (2013) Experimental constraints on the thermodynamics and sound velocities of hcp-Fe to core pressures. Journal of Geophysical Research: Solid Earth, 118, 1999–2016.
Mutch, E.J.F., Blundy, J.D., Tattitch, B.C., Cooper, F.J., and Brooker, R.A. (2016) An experimental study of amphibole stability in low-pressure granitic magmas and a revised Al-in-hornblende geobarometer. Contributions to Mineralogy and Petrology, 171, 1–27.
Nasir, S., and Al-Rawas, A.D. (2006) Mössbauer characterization of upper mantle ferrikaersutite. American Mineralogist, 91, 1163–1169.
Ni, P., Zhang, Y., and Guan, Y. (2017) Volatile loss during homogenization of lunar melt inclusions. Earth and Planetary Science Letters, 478, 214–224.
Oberti, R., Hawthorne, F.C., Cannillo, E., and Cámara, F. (2007) Long-range order in amphiboles. Reviews in Mineralogy and Geochemistry, 67, 125–171.
Oberti, R., Boiocchi, M., Zema, M., Hawthorne, F.C., Redhammer, G.J., Susta, U., and Della Ventura, G. (2018) The high-temperature behaviour of riebeckite:

expansivity, deprotonation, selective Fe oxidation and a novel cation disordering scheme for amphiboles. European Journal of Mineralogy, 30, 437–449.
Ohira, I., Jackson, J.M., Sturhahn, W., Finkelstein, G.J., Kawazoe, T., Toellner, T.S., Suzuki, A., and Ohtani, E. (2021) The influence of δ-(Al,Fe)OOH on seismic heterogeneities in Earth's lower mantle. Scientific Reports, 11, 9.
Pallister, J.S., Hoblitt, R.P., Meeker, G.P., Knight, R.J., and Siems, D.F. (1996) Magma mixing at Mount Pinatubo: petrographic and chemical evidence from the 1991 deposits. Fire and mud: eruptions and lahars of Mount Pinatubo, Philippines, 687–731.
Pallister, J.S., Thornber, C.R., Cashman, K.V., Clynne, M.A., Lowers, H., Mandeville, C.W., Brownfield, I.K., and Meeker, G.P. (2008) Petrology of the 2004–2006 Mount St. Helens lava dome–Implications for magmatic plumbing and eruption triggering. A Volcano Rekindled: The Renewed Eruption of Mount St. Helens, 2004–2006. U.S. Geological Survey Professional Paper, 1750, 2330–7102.
Peters, S.T., Troll, V.R., Weis, F.A., Dallai, L., Chadwick, J.P., and Schulz, B. (2017) Amphibole megacrysts as a probe into the deep plumbing system of Merapi volcano, Central Java, Indonesia. Contributions to Mineralogy and Petrology, 172, 1–20.
Phillips, M.W., Draheim, J.E., Popp, R.K., Clowe, C.A., and Pinkerton, A.A. (1989) Effects of oxidation-dehydrogenation in tschermakitic hornblende. American Mineralogist, 74, 764–773.
Popp, R.K., Phillips, M.W., and Harrell, J.A. (1990) Accommodation of Fe^{3+} in natural, Fe^{3+}-rich, calcic and subcalcic amphiboles; Evidence from published chemical analyses. American Mineralogist, 75, 163–169.
Prouteau, G., and Scaillet, B. (2003) Experimental constraints on the origin of the 1991 Pinatubo dacite. Journal of Petrology, 44, 2203–2241.
Redhammer, G., and Roth, G. (2002) Crystal structure and Mössbauer spectroscopy of the synthetic amphibole potassic-ferri-ferrorichterite at 298 K and low temperatures (80–110 K). European Journal of Mineralogy, 14, 105–114.
Ridolfi, F. Zanetti, A., Renzulli, A., Perugini, D., Holtz, F., and Oberti, R. (2018) AMFORM, a new mass-based model for the calculation of the unit formula of amphiboles from electron microprobe analyses. American Mineralogist, 103, 1112–1125.
Scaillet, B., and Evans, B.W. (1999) The 15 June 1991 eruption of Mount Pinatubo. I. Phase equilibria and pre-eruption *P-T-*f_{O_2}*-f* H_2O conditions of the dacite magma. Journal of Petrology, 40, 381–411.
Schmidbauer, E., Kunzmann, T., Fehr, T., and Hochleitner, R. (2000) Electrical resistivity and ^{57}Fe Mössbauer spectra of Fe-bearing calcic amphiboles. Physics and Chemistry of Minerals, 27, 347–356.
Semet, M.P. (1973) A crystal-chemical study of synthetic magnesiohastingsite. American Mineralogist, 58, 480–494.
Shaw, A., Hauri, E., Fischer, T., Hilton, D., and Kelley, K. (2008) Hydrogen isotopes in Mariana arc melt inclusions: Implications for subduction dehydration and the deep-Earth water cycle. Earth and Planetary Science Letters, 275, 138–145.
Solomatova, N.V., Jackson, J.M., Sturhahn, W., Rossman, G.R., and Roskosz, M. (2017) Electronic environments of ferrous iron in rhyolitic and basaltic glasses at high pressure. Journal of Geophysical Research: Solid Earth, 122, 6306–6322.
Solomatova, N.V., Alieva, A., Finkelstein, G.J., Sturhahn, W., Baker, M.B., Beavers, C.M., Zhao, J., Toellner, T.S., and Jackson, J.M. (2019) High-pressure single-crystal X-ray diffraction and synchrotron Mössbauer study of monoclinic ferrosilite. Comptes Rendus Geoscience, 351, 129–140.
Sturhahn, W. (2000) CONUSS and PHOENIX: Evaluation of nuclear resonant scattering data. Hyperfine Interactions, 125, 149–172.
——— (2004) Nuclear resonant spectroscopy. Journal of Physics: Condensed Matter, 16, S497–S530.
——— (2005) Nuclear resonant scattering. In F. Bassani, G.L. Liedl, and P. Wyder, Eds., Encyclopedia of Condensed Matter Physics, p. 227–234. Elsevier.
——— (2021) CONUSS (COherent NUclear Scattering by Single crystals). Open source software. http://www.nrixs.com.
Sturhahn, W., and Gerdau, E. (1994) Evaluation of time-differential measurements of nuclear-resonance scattering of X-rays. Physical Review B, 49, 9285–9294.
Sturhahn, W., and Jackson, J.M. (2007) Geophysical applications of nuclear resonant spectroscopy. Geological Society of America Special Papers, 421, 157.
Taylor, L.A., Logvinova, A.M., Howarth, G.H., Liu, Y., Peslier, A.H., Rossman, G.R., Guan, Y., Chen, Y., and Sobolev, N.V. (2016) Low water contents in diamond mineral inclusions: Proto-genetic origin in a dry cratonic lithosphere. Earth and Planetary Science Letters, 433, 125–132.
Thornber, C.R., Pallister, J.S., Lowers, H.A., Rowe, M.C., Mandeville, C.W., and Meeker, G.P. (2008) Chemistry, mineralogy, and petrology of amphibole in Mount St. Helens 2004–2006 dacite. A Volcano Rekindled: The Renewed Eruption of Mount St. Helens, 2004–2006. U.S. Geological Survey Professional Paper.
Toellner, T.S. (2000) Monochromatization of synchrotron radiation for nuclear resonant scattering experiments. Hyperfine Interactions, 125, 3–28.
Toellner, T., Alp, E., Graber, T., Henning, R., Shastri, S., Shenoy, G., and Sturhahn, W. (2011) Synchrotron Mössbauer spectroscopy using high-speed shutters. Journal of Synchrotron Radiation, 18, 183–188.
Treiman, A.H., Boyce, J.W., Greenwood, J.P., Eiler, J.M., Gross, J., Guan, Y., Ma, C., and Stolper, E.M. (2016) D-poor hydrogen in lunar mare basalts assimilated from lunar regolith. American Mineralogist, 101, 1596–1603.
Turrin, B.D., Christiansen, R.L., Clynne, M.A., Champion, D.E., Gerstel, W.J., Patrick Muffler, L., and Trimble, D.A. (1998) Age of Lassen Peak, California, and implications for the ages of late Pleistocene glaciations in the southern Cascade Range. Geological Society of America Bulletin, 110, 931–945.
Underwood, S., Feeley, T., and Clynne, M. (2012) Hydrogen isotope investigation of amphibole and biotite phenocrysts in silicic magmas erupted at Lassen Volcanic Center, California. Journal of Volcanology and Geothermal Research, 227-228, 32–49.
——— (2013) Hydrogen isotope investigation of amphibole and glass in dacite magmas erupted in 1980–1986 and 2005 at Mount St. Helens, Washington. Journal of Petrology, 54, 1047–1070.
Uvarova, Y., Sokolova, E., Hawthorne, F., McCammon, C., Kazansky, V., and Lobanov, K. (2007) Amphiboles from the Kola Superdeep Borehole: Fe^{3+} contents from crystal-chemical analysis and Mössbauer spectroscopy. Mineralogical Magazine, 71, 651–669.
Vandenberghe, R.E., and De Grave, E. (2013) Application of Mössbauer spectroscopy in Earth Sciences. In Y. Yoshida and G. Langouche, Mössbauer Spectroscopy, p. 91–185. Springer.
Vennemann, T.W., and O'Neil, J.R. (1996) Hydrogen isotope exchange reactions between hydrous minerals and molecular hydrogen: I. A new approach for the determination of hydrogen isotope fractionation at moderate temperatures. Geochimica et Cosmochimica Acta, 60, 2437–2451.
Walowski, K.J., Wallace, P.J., Hauri, E., Wada, I., and Clynne, M.A. (2015) Slab melting beneath the Cascade Arc driven by dehydration of altered oceanic peridotite. Nature Geoscience, 8, 404–408.
Zou, B., and Ma, C. (2020) Crystal mush rejuvenation induced by heat and water transfer: Evidence from amphibole analyses in the Jialuhe Composite Pluton, East Kunlun Orogen, northern Tibet Plateau. Lithos, 376-377, 105722.

Manuscript received April 23, 2021
Manuscript accepted December 16, 2021
Accepted manuscript online December 22, 2021
Manuscript handled by Charles A. Geiger

Endnote:

[1]Deposit item AM-23-18115, Online Materials. Deposit items are free to all readers and found on the MSA website, via the specific issue's Table of Contents (go to http://www.minsocam.org/MSA/AmMin/TOC/2023/Jan2023_data/Jan2023_data.html).